The upper-thermal stability of an iron-rich smectite: implications for smectite formation on Mars

Brittany M. DePasquale, David M. Jenkins[1]

Department of Geological Sciences and Environmental Studies, Binghamton University, Binghamton, New York, 13902-6000

[1]Corresponding author: David M. Jenkins; dmjenks@binghamton.edu

Abstract

Fe-rich smectite is a clay mineral commonly found on Mars, particularly in the lowest stratigraphic sequences. The presence of smectite is of interest because of its implications for the former presence of water in the near-surface environment. What is unclear are the range of bulk compositions and physical conditions under which this smectite formed. Here we investigated (i) the experimental synthesis of iron-rich tri-octahedral smectite (Fe-smectite) from a variety of bulk chemical compositions, primarily along the Fe-talc—Na-Fe-eastonite join, and (ii) the upper-thermal stability of Fe-smectite made from one of the investigated bulk compositions. It was found that Fe-smectite could be synthesized at 500°C and 2 kbars in 7-10 days from all of the bulk compositions investigated, demonstrating some flexibility in the compositions of rock and soil on Mars that would yield Fe-smectite. The upper-thermal stability of the Fe-smectite synthesized from the bulk composition consisting of 87 mol% Fe-talc was investigated in the range of 1-3 kbar and 530-620°C. Breakdown of this smectite (without interlayer water) was modeled thermodynamically by a dehydration reaction involving albite, fayalite, hercynite, quartz, magnetite, and water to permit extrapolation to lower pressures and temperatures. Results from this modeling indicate first that Fe-smectite is stable to depths of 30 km, for a geothermal gradient of 20°C/km during the Noachian period, indicating that, even without any interlayer water, Fe-smectite has potential for storing considerable amounts of water in the crust of Mars. Second, there is no overlap in the upper-thermal stability of Fe-smectite and the water-saturated solidus of basalt, ruling out direct formation from a basaltic magma for this Mg-free smectite. Third, the upper-thermal stability of Fe-smectite is calculated to be 336 ± 25 °C at 100

bars, which is above the liquid-vapor boundary for H_2O, suggesting that formation in the presence of a primordial dense vapor phase in the earliest history of Mars is possible.

Keywords: Fe-smectite, Mars, thermal stability, thermodynamics, clay minerals

1 Introduction

Smectite is an expandable phyllosilicate (e.g., Moore and Reynolds, 1997, p. 155; Kloprogge et al., 1999) that contains variable proportions of Al, Mg, and Fe, particularly in the octahedral sites (Bishop et al., 1999). It can exist as a dioctahedral or trioctahedral sheet silicate (Michalski et al., 2015). Of particular interest are iron-rich smectites as they are commonly found on Mars (Poulet et al., 2005; Ehlmann et al., 2011, 2013; Carter et al., 2015, Michalski et al., 2015; Bristow et al., 2018). On Mars, Fe- and Mg-rich phyllosilicates comprise about 89% of the H_2O- and OH-bearing phases observed directly by rovers and remotely by orbiters using visible and near-infrared reflectance spectroscopy (Chemtob et al., 2017). Ferric-iron rich dioctahedral smectite (nontronite) is believed to form from oxidation of ferrous-iron-rich trioctahedral smectites (Chemtob et al., 2015, 2017; Cannon et al., 2017), such that nontronite on Mars may be the oxidized version of a more reduced precursor trioctahedral smectite. The detailed crystal chemistry and origin of phyllosilicates on Mars are, however, largely unknown (Baron et al., 2019). Smectite in this study, unless otherwise indicated, will refer to the Fe^{2+}-Mg-trioctahedral rich variety

Figure 1 shows a selection of ferrous-Fe-rich smectite compositions, where the mole fraction of Mg on the octahedral sites is less than 0.5, found on Earth or made experimentally to provide some basis for understanding the compositional variations for these minerals. Smectite compositions are plotted as mol% of the components Na+K+Ca,

Al, and Fe_{total}. In general these smectites range from having nearly equal parts Fe and Al to being distinctly Fe rich. The proportion of interlayer cations is usually quite low, and appears to decrease going toward the Fe_{total} corner of the diagram. The majority of natural smectite samples plotted on this diagram appear to fall near the join between Fe-talc ($Fe_3Si_4O_{10}(OH)_2$) and Na-Fe-eastonite ($Na(FeAl_2)(Al_3Si)O_{10}(OH)_2$). These end-member phyllosilicate minerals were chosen for comparison on this plot simply because they span the compositional range of interest.

On Earth, smectite is generally found near mafic localities such as basalt (Curtin and Smillie, 1981), in serpentinized ultramafic rocks (Nguyen-Thanh et al., 2014), and is formed as an authigenic mineral in marine sediment or as a result of hydrothermal alteration in low temperature settings (Charpentier et al., 2011). It has also been found mixed with carbonate sediments in the deep ocean where replacement of pyrite by smectite occurs (Gaudin et al., 2005) and is commonly found near hydrothermal vents. Dioctahedral smectite has been found in higher temperature settings than trioctahedral smectite and is often found near black or white smokers on the ocean floor rather than in regions with cooler hydrothermal fluids (Charpentier et al., 2011).

Iron-rich smectites are commonly found on Mars and can offer insight into its climate history (Poulet et al., 2005; Michalski et al., 2015), as well as potential information on the possibility of life there (Bristow et al., 2018). The presence of an active hydrologic cycle on early Mars is supported by the presence of clay minerals, which can contain interlayer water. Their presence may indicate a time in the past when the climate was wetter with alkaline or near-neutral conditions before evolving to an era that was drier with surface waters that were more acidic (Ehlmann et al., 2011), leading

to a gradual decrease in smectite formation (Ehlmann et al., 2013). However, other studies (Peretyazhko et al., 2018) noted the widespread occurrence of smectite without coexisting carbonates and suggested that the smectite formed in acidic conditions during the early history of Mars, perhaps by outgassing of SO_2 during periods of high volcanic activity in the Noachian or early Hesperian eras.

Ehlmann et al. (2013) proposed seven settings that would lead to the formation of hydrated silicates starting with a basaltic precursor. Four of these settings involved elevated temperatures, namely, hydrothermal circulation driven by volcanic or impact heat sources, deep-seated metamorphism, and from fluids evolving from a crystallizing or differentiating magma. Recognizing that smectite formation is often controlled by kinetics or reaction pathways (Ehlmann et al., 2013; Baron et al., 2019), it is still useful to consider the equilibrium formation of smectite as a point of reference, even if investigated at temperatures well above those encountered in near-surface environments. Defining the upper-thermal stability of Fe-Mg-smectite in reaction-reversal experiments can (i) provide lower limits on the temperatures at which Fe-rich smectite forms, and (ii) permit the extraction of thermochemical data which, in turn, can be used to extrapolate high-temperature results more reliably to lower-temperature regions that are less amenable to direct experimental investigation.

The majority of experimental work on Fe-rich smectite has been done at relatively low pressures (P = liquid-vapor saturation) and temperatures (T = 3-350 °C) to explore the conditions needed for its synthesis. Kloprogge et al. (1999) reviewed earlier work on the synthesis of smectite where it can be seen that most earlier attempts working with Fe-

smectite resulted largely in making ferric-iron (dioctahedral) nontronite (e.g., Harder, 1978; Decarreau and Bonnin, 1986).

More recently, Chemtob et al. (2015) developed a method for synthesizing ferrous-Fe-smectite that involved a variation of the method used by Decarreau and Bonnin (1986). Chemtob et al. (2015) used Fe^{2+}-Mg-Al-silicate gels as starting materials which were then treated under anoxic conditions at 200°C and at vapor-saturation conditions for 15 days. They prepared ferrous-smectites over a wide range of $Fe/(Fe^{2+}+Mg)$ ratios. These same materials were then studied by Chemtob et al. (2017) to determine if these ferrous smectites could be oxidized to nontronite when exposed to air-saturated solutions or in hydrogen peroxide (0.2% H_2O_2) solutions. In both cases, the ferrous iron was substantially oxidized to ferric iron (nontronite component), especially when treated in the hydrogen peroxide solution. In both studies, the authors noted the unintentional oxidation of ferrous-smectite to occur even when stored in nominally anaerobic chambers, indicating the oxidation of ferrous-smectite is kinetically favorable. This also suggests that nontronite observed today on Mars may indeed have started as trioctahedral ferrous-smectite or Fe-saponite as observed by direct sampling at Gale crater on Mars (Vaniman et al., 2014; Bristow et al., 2018).

Cannon et al. (2017) proposed that clay minerals on Mars may have formed soon after the accretion of Mars when there might have been a very dense and hot atmosphere present to react with a basaltic crust. They studied the interaction between a Martian-analogue basalt and H_2O or mixed H_2O-CO_2 atmospheres over a range of conditions (325-425 °C and 150-300 bars) such that the ambient fluid was present as either a liquid, vapor, or supercritical fluid. A variety of Fe-rich trioctahedral clay minerals formed

depending on the treatment conditions. For example, basalt treated at 425°C and 300 bars with a supercritical H_2O-CO_2 mixture formed trioctahedral sheet silicates with a 14Å basal reflection indicative of montmorillonite or vermiculite. Their study showed that liquid water might not have been required to form clay minerals on Mars. Instead, an atmosphere rich in steam would have been sufficient to alter basalt to form a layer of clay minerals at the surface.

Peretyazhko et al. (2018) noted the limited occurrences of carbonate deposits on Mars, which stood in contrast to the widespread occurrence of smectite, and proposed that the clay minerals were formed in conditions that were too acidic for carbonates to be deposited. Accordingly, Peretyazhko et al. (2018) tested this hypothesis by investigating whether phyllosilicates would form from a Mars-analogue basalt treated in the presence of variable H_2SO_4 concentrations. Vapor-saturation pressure conditions were chosen along with a maximum temperature of 200°C. This study determined that after 14 days of incubation dioctahedral smectite formed at low pH (~3) and trioctahedral smectite formed at pH conditions greater than 4. The recent work by Baron et al. (2019) shows that the dioctahedral smectite Na-nontronite is ultimately unstable relative to the phases aegirine (a pyroxene) and hematite when treated in NaOH solutions with initial pH values of 12 and13.3 at 150 °C and at vapor-saturation conditions for up to 183 days. This latter study places upper limits on the pH at which dioctahedral smectite would form on Mars.

To complement these existing studies, we provide here a two-part experimental study of smectite formation. The first is a reconnaissance study of smectite synthesis using a range of bulk compositions to provide some indication of the tolerance of smectite formation to the bulk chemical composition of the starting material, while the

second (and larger) part of this work is a study of the upper-thermal stability of trioctahedral Fe-rich smectite from one specific bulk composition. The latter establishes the equilibrium boundary between an Fe-smectite and its breakdown products using the method of reaction reversals, as compared to the synthesis of smectite which may or may not be kinetically controlled (Baron et al., 2019). There are two primary goals to the second part of this study: (1) determine upper-limits on the temperature at which a trioctahedral Fe-smectite could form by hydrothermal activity on Mars, and (2) extract thermochemical data for this smectite to allow extrapolation of the results obtained at relatively high *P*-*T* conditions to much lower conditions.

2 Methods

2.1 Starting materials. Smectite was synthesized from mixtures of reagent-grade SiO_2, Al_2O_3, Fe_2O_3, Fe°, and Na_2CO_3. The SiO_2 was made by desiccating silicic acid hydrate ($SiO_2 \cdot nH_2O$) to a constant mass-loss weight by heating at 1 atm in steps to 1100°C and holding at this temperature for approximately 24 hours. The resultant SiO_2 (cristobalite, confirmed by XRD) was placed in a desiccator to cool before the sintered charge was ground by hand in an agate mortar to a finer powder for ease of handling.

Fe-smectite mixtures were prepared by first weighing SiO_2, Na_2CO_3, and Al_2O_3 in the desired proportions and mixing by hand for approximately 20 minutes under acetone until dry. This mixture was then decarbonated in air at 900°C for 15 minutes. Fe_2O_3 and Fe° (~ 10 μm powder) were then added in the molar ratio of 1:2 so that they would chemically equate to FeO. The iron-bearing reagents and the decarbonated SiO_2-Na_2O-Al_2O_3 mixture were then mixed dry (without acetone) by hand for approximately 20

minutes to prevent the Fe from settling out of the mixture and yielding a mixture with no visible segregation.

A series of compositions was investigated in a reconnaissance manner to determine whether or not smectite would form, and, if so, which bulk composition yielded the highest amount of Fe-rich smectite. Two compositions, namely $Na(Fe_3)(AlSi_3)O_{10}(OH)_2$ (Smec1) and $Na_{0.4}(Fe_{1.8}Al_{0.8}\square_{0.4})(Al_{0.4}Si_{3.6})O_{10}(OH)_2$ (Smec2), where □ represents a vacancy, were chosen initially based on previous results obtained in Fe-free (Mg-rich) systems (Carman, 1974; Basora et al., 2012). The former composition is the ferrous-iron equivalent of aspidolite ($NaMg_3(AlSi_3)O_{10}(OH)_2$, or Na-phlogopite) which had been studied extensively by Carman (1974), while the second is modeled after the smectite composition determined by Basora et al. (2012). In addition, a series of starting mixtures were prepared along the join Na-Fe-eastonite ($Na(FeAl_2)(Al_3Si)O_{10}(OH)_2$) and Fe-talc ($Fe_3Si_4O_{10}(OH)_2$). Five mixtures were made consisting of 69, 75, 81, 87, and 91 mole % Fe-Talc. These compositions were chosen based on their proximity to natural and previously synthesized Fe-smectite compositions as plotted on an Al, Na, Fe ternary diagram (Figure 2). Table 1 lists the bulk compositions, expressed as the sheet silicates with ideal structural OH contents, of the mixtures investigated in this study.

2.2 Experimental methods. All experiments were done in the range of 500-700 °C and 1-3 kbar pressure, conditions that yield relatively rapid reaction rates and which comprise the growth and breakdown of the Fe-rich smectite studied here. Silver-palladium ($Ag_{50}Pd_{50}$) capsules were used in experiments due to its low reactivity with Fe (e.g., Driscall et al., 2005) and high permeability to H_2 (Chou, 1986). Capsules used for

synthesis purposes were made from $Ag_{50}Pd_{50}$ tubing with a 4 mm outer diameter and 0.13 mm wall thickness cut to 1.2 cm lengths and cleaned with acetone. The section of tubing was then flame annealed and one end was crimped and arc-welded closed under a damp tissue. Approximately 80 mg of starting material was added to each capsule. Deionized water was then added to the capsule using a micro-syringe in an amount approximately equal to 10% of the weight of the solid, which is sufficient to provide H_2O for the formation of smectite and to facilitate cation transport between the solid phases. The open end of the capsule was crimped and arc-welded shut to create a closed capsule.

Experiments on the upper-thermal stability of smectite used reversal mixtures consisting of the products of two previous treatments, one being from an experiment that produced smectite at 500°C, while the other was from one that produced only the breakdown products at 700°C, namely quartz, fayalite, hercynite, ± albite. This type of experimental mixture, which has both reactant and product phases present, should minimize nucleation barriers in locating this reaction boundary. Reversal reaction experiments were prepared in a similar manner to that used for the synthesis experiments, where capsules were made from $Ag_{50}Pd_{50}$ tubing with 1.5 mm outer diameter and 0.13 mm wall thickness. Capsules were 0.6 mm long and contained approximately 4 mg of starting reversal mixture. To this was added approximately 10% deionized water relative to the amount of solid material.

Experiments at 1-2 kbar were done in cold-seal pressure vessels. Uncertainties in pressure and temperature are approximately ± 0.05 kbars and ± 5°C, respectively (Jenkins, 1987). A 1-centimeter length of 0.3 cm diameter iron rod was added to the cold-seal vessel, made of René 41, in order to act as an oxygen getter to reduce the fO_2

around the capsule (see below). The capsule was then placed in the apparatus and an additional filler rod, also made of René 41, was inserted after the capsule and iron rod in order to fill void space in the vessel. The vessel was then pressurized with water and heated for 2-14 days before being quenched. After quenching, the capsule was removed from the vessel and weighed before a small incision was made in the capsule to allow any excess water to be evaporated from the capsule. It was then dried in a furnace at 160°C for 10-15 minutes and weighed again to determine the water content in the capsule. The samples were then ground to a fine powder and placed in vials until analyzed by X-ray diffraction and electron microprobe.

The fO_2 in the cold-seal experiments was controlled in a general way by the reaction of the iron rod with the water used to pressurize the system. This reaction reduced the fO_2 of the system at 2 kbars and 700°C to $\log fO_2$ of -18.1 to -17.7 (Chan et al., 2016). This is approximately 1 $\log(fO_2)$ below the fayalite-magnetite-quartz (FMQ) buffer or 1.5-1.9 $\log(fO_2)$ units below the Ni-NiO buffer. However, at the lower temperatures used for the reaction reversal experiments of this study (530-650 °C) the fO_2 was very close to the FMQ boundary, as evidenced by the nearly constant presence of fayalite, magnetite, and quartz in the reaction products. These oxidation conditions are near the upper range estimated from Martian meteorites (Tuff et al., 2013; Righter et al., 2020) and are probably reasonable for the near-surface environment on early (greater than 3.7 Ga) Mars (Tuff et al., 2013).

Another set of experiments, conducted at 3 kbars, was done in internally-heated gas vessels. In this setup, the capsule was placed inside a nichrome-wound furnace between two thermocouples to assess any temperature gradient along the length of the

capsule. The capsule was held in place between the thermocouple tips by a copper cylinder that was then filled with silica wool. Generally, the temperature gradient observed was ~5°C. Uncertainties in pressure are approximately ± 0.05 kbars based on bourdon-tube gauge accuracy, as checked against a Harwood Engineering factory-calibrated manganin cell, excluding any pressure variation during the treatment.

Hydrogen fugacity in the gas vessels was used to adjust the fO_2 in the capsule to that near the FMQ buffer using hydrogen-argon mixtures as the pressure medium. The hydrogen fugacity (fH_2) was established by initially pressurizing the system (gas vessel and pressure intensifier) with a given pressure of H_2 and then pumping the system with argon to a predetermined total pressure of H_2 + Ar to achieve a given mole fraction of H_2 (typically around 0.002) at a total pressure of about 1.8 kbar. The final pressure of 3.0 kbars was reached through thermal expansion. After quenching, the capsules were treated the same as they were after being removed from the cold-seal vessels to determine their water content.

2.3 Analytical methods. Powder X-ray diffraction (XRD) was done using a Panalytical Xpert PW3040-MPD diffractometer. Most scans were made in air at ambient room temperatures and humidity using CuKα radiation generated at 40 kV and 20 mA. Samples were ground to a powder following treatment and were then mounted as a thin smear on zero-background quartz plates. They were scanned from 5 to 70°2θ in order to capture a large range of known smectite peaks. The most prominent smectite peak is the (001) occurring around 6-7°2θ. The location of this peak is dependent on humidity at the time of the scan, shifting toward higher angles (7° 2θ) when the relative humidity is lower, indicating that there is less interlayer water present in the sample. Aside from the

humidity-dependent location of the (001), there was no indication of any obvious oxidation of the smectite during ambient (room temperature) scans as might be observed by shifts in peak positions (e.g., Chemtob et al., 2017) from duplicate scans. Unit-cell dimensions were obtained by Rietveld refinements using GSAS II (Toby and Von Dreele, 2013). Some scans were made at high temperatures (in air) using an Anton Paar HTK-10 high-temperature stage.

A JEOL-8900 was used for back-scattered electron imaging and electron microprobe analysis. Experimental products were dispersed in epoxy (Petropoxy 154®) and cured in air at 100°C. The cured epoxy mounts were polished on fiber laps impregnated with diamond grit and ethylene glycol in steps down 0.5 µm. Polished samples were then ultrasonically cleaned in water before being coated with carbon. The microprobe was operated at 15 kV and 10 nA, the same operating conditions as those used to characterize saponite by Treiman et al. (2014). Owing to the small grain sizes (2 x 5 µm cross sections, Fig. 3), samples were analyzed using a focused beam but counting for only 10 sec on the peak and 3 sec on the background positions to minimize Na diffusion under the beam. In the absence of a phyllosilicate standard, the oxides Fe_2O_3, Al_2O_3, and SiO_2 were used for Fe, Al, and Si, respectively, and albite ($NaAlSi_3O_8$) for Na as reasonable silicate mineral standards that minimize element matrix corrections and wavelength shifts (Reed, 1996, p. 160). Matrix corrections employed the ZAF correction scheme (e.g., Reed, 1996, p. 134-140).

3 Results

3.1 Smectite synthesis

The results of smectite synthesis experiments, all done at 500°C and 2 kbars for 7-10 days, are listed in Table 2. Analysis by XRD indicated that all seven bulk compositions, including the five along the Na-Fe-eastonite—Fe-talc join, gave at least partial yields of smectite, generally forming along with magnetite, fayalite, quartz, and minor albite (Table 2). Formation of smectite over this relatively wide range of bulk compositions suggests that Fe-rich smectite formation on Mars could occur from a reasonably wide range of rock or soil compositions.

The bulk composition producing the largest amount of smectite was chosen for determining its upper-thermal stability. This was done by a simple comparison of the peak height of the smectite reflection at 6-7° 2θ to the peak height of quartz, both of which were prominent in each of the five compositions along the join Na-Fe-eastonite—Fe-talc. Accordingly, the highest smectite yield occurred for sample FTC87 (Table 2), which was chosen for further study.

3.2 Smectite characterization

Figure 3 is a representative electron-backscattered image of the synthetic smectite made in this study. Smectite forms with micaceous habit, here seen in cross section in these epoxy mounted and polished samples. It frequently opens up under the electron beam, forming voids between the sheets as heat from the electron beam drives water molecules from interlayer sites. Magnetite is seen as small brighter grains and quartz as larger anhedral darker grains in this image.

A comparison of several room-temperature and high-temperature XRD scans focusing on the (001) reflection of smectite is given in Figure 4. The top two patterns were both measured at room temperature but show a distinct difference in the (001) position. The top pattern corresponds to bi-hydrated smectite with 2 planes of interlayer water (d_{100} = 14.8 Å, 2L) while the second pattern corresponds to mono-hydrated smectite with 1 plane (d_{100} = 12.2-12.4 Å, 1L) (Ferrage, 2016). The top pattern was obtained during the late spring when the relative humidity (RH) and dew point (T_d) in the lab were higher, typically 50% and 15°C respectively, while the second pattern was obtained during the late fall when the RH and T_d were about 30% and 1°C, respectively. With increasing temperature of the XRD measurements, the (001) shifts to that consistent with zero interlayer water (d_{100} = 10.3-10.4 Å, 0L) indicating that dehydration occurs in the range of 100-150 °C, or 125 ± 25°C. Unlike Mg-rich smectite which immediately rehydrates upon cooling back to room temperature (Jenkins and Corona, 2006), Fe-rich smectite does not. Instead it remains in a state with no interlayer water at least for the duration of the XRD scan (~30 min).

Electron microprobe analysis of the synthetic smectite made from the bulk compositions Smec1, Smec2, and FTC87 are listed in Table 3. Allowing for the presence of H_2O as both intralayer OH and interlayer H_2O, one would expect analytical totals of 89-92 wt% for water present at a total of 2-3 H_2O per 11 oxygens. As can be seen in Table 3 the analytical totals are generally lower than this. The issue of low analytical totals from the electron microprobe analysis of fine-grained synthetic materials has been studied at length in this lab (e.g., Giblin et al., 1993; Jenkins and Corona, 2006) where it has been found that analyses with analytical totals as low as 65-70 wt% will give

acceptable stoichiometries that are essentially equivalent to coarse-grained materials. The analytical totals observed here are above this lower limit.

A portion of the synthesis products from FTC87-1 (Table 2) was treated with ethylene glycol to confirm the presence of smectite compared to other swelling clays (e.g., vermiculite). The sample was ground to a powder in an agate mortar and pestle. The powder was then mounted on a glass plate using acetone to create a relatively even smear, placed in a desiccator just above ethylene glycol (EG), and heated in an oven at 60°C for 4 hours. Analysis of the EG-treated sample showed the d_{001} was shifted to 16.7Å. This indicates the sheet silicate is indeed smectite as EG-treated samples show a d-spacing in the range of 16.5 to 17.3Å (Srodon, 1980; Szczerba and Ufer, 2018).

The volume of smectite with no interlayer water was determined by Rietveld refinement of the high-temperature pattern for FTC87-5 (Fig. 4). Based on the earlier work of Carman (1974), who showed that all interlayer water is lost at 350-400°C and occurs nearly isothermally over a wide range of pressure, it is presumed the smectite of this study also loses all interlayer water prior to reaching its breakdown temperature (> 500 °C). Refinements were initiated by using the structure of Na-vermiculite from Slade et al. (1985), with interlayer water reduced to essentially nothing. Additional phases included quartz (Levien et al., 1980), fayalite (Birle et al., 1968), magnetite (Wechsler et al., 1984), and aluminum (from the heating stage mount). The unit cell volume for smectite was determined to be 507.2 ± 3.0 $Å^3$ with the large uncertainty stemming from the strong preferred orientation and moderate amount of smectitie in the sample. The resultant molar volume of 152.7 ± 0.9 cm^3/mol (Z = 2) is intermediate to that of ferro-

talc (142.25 cm^3/mol) and annite (154.30 cm^3/mol) reported by Holland and Powell (2011) which is broadly consistent with the composition of smectite for this study.

3.3 Reversal experiments

Reaction reversal experiments were used to determine the upper-thermal stability of the Fe-smectite formed in this study over the range of 1 – 3 kbar and 530-650°C, conditions where the reaction rates were found to be relatively rapid. Results from the reversal experiments are listed in Table 4 and plotted in Figure 5. The smectite stability field at pressures of 1 – 3 kbar was readily determined by a simple comparison of the relative peak heights of the major peaks in the XRD patterns before and after, where the low-angle reflection of smectite (6-7° 2θ) served as a clear indication of its growth or breakdown (Figure 6). The boundary shown in Figure 5 is drawn by eye; a boundary based on a thermodynamic analysis of the data reported here will be presented below. Regardless of whether smectite grew or broke down, abundant quartz, fayalite, magnetite, hercynite, and minor albite were frequently found coexisting in the assemblage.

3.4 Analysis of phases in reversal experiments

Analyses of the reaction reversal experiments were preformed to determine primarily the composition of smectite, with additional analyses of magnetite and hercynite, as these are the only phases that could experience significant solid solution in this chemical system. Selected analyses of the smectite formed in smectite-growth experiments are given in Table 3 and shown in Figure 7. Shown also in Figure 7 is the analysis of the smectite used in the starting mixture (solid circle), as well as the bulk composition of the mixture FTC87-1 (crossed circle) used to make the starting-material smectite. All of the smectite analyses plot very close to each other and at significantly

lower Fe contents than that of the bulk composition. The low Fe content in smectite is balanced by the appearance of magnetite, which would plot at the Fe corner of this truncated ternary diagram. Given the lack of any obvious variation in the composition of the reaction-product smectites from that of the starting material, the compositions of all the smectites formed from the FTC87 bulk composition were averaged together and shown in the last column of Table 3. The smectite formula based on the averaged analyses is $Na_{0.23}(Fe^{2+}_{2.05}Fe^{3+}_{0.50}Al_{0.45})(Al_{1.18}Si_{2.82})O_{10}(OH)_2 \cdot nH_2O$. The ferric iron content was estimated by summing the octahedral Al, Fe^{2+}, and Fe^{3+} to equal 3, giving fully occupied octahedral sites and which also limits Fe from residing on the interlayer sites.

Magnetite and hercynite were also analyzed in these samples. Both magnetite and hercynite commonly occurred together, but there was a tendency for magnetite to grow or be dominant in smectite-growth experiments (e.g., FTC87R-8), while hercynite was dominant in smectite-breakdown experiments (e.g., FTC87R-1). Representative electron microprobe analyses of magnetite and hercynite are listed in Table 5. In this chemical system, one would expect spinel to form primarily along the magnetite-hercynite ($Fe^{2+}Fe^{3+}{}_2O_4$-$FeAl_2O_4$) join and, at these temperatures, with only limited solid solution (Turnock and Eugster, 1962; Golla-Schindler et al., 2005); however, minor amounts of Si were consistently observed. The presence of Si in spinel is a topic of ongoing research, where improved TEM methods are helping to resolve whether the Si occurs in solid solution or as nanoscale inclusions of spinel-structured (cubic) Si-rich phases, such as Fe_2SiO_4 in the spinel structure and $Fe_{1.5}SiO_4$ in the maghemite structure (e.g., Ciobanu et al., 2019), and whether these are possibly exsolution or primary precipitate phases. In

this study, we are assuming that the minor Si is present in solid solution as Fe_2SiO_4. The electron microprobe analyses were then recast as follows. Cations were first calculated on the basis of 4 oxygens assuming all iron is Fe^{2+}. Then, Fe^{2+} was assigned to Al^{3+} and Si^{4+} as the spinel components hercynite ($FeAl_2O_4$) and ahrensite (Fe_2SiO_4), respectively, with the remaining Fe^{2+} partitioned as 1/3 Fe^{2+} and 2/3 Fe^{3+} into the magnetite ($FeFe^{3+}{}_2O_4$) component. All cations were then renormalized based on 4 oxygens to a total of 3 cations. Because of the relative chemical simplicity of this system, the lattice parameters of the spinels afforded a cross check on the microprobe analyses. Using the magnetite structure of Wechsler et al. (1984) and hercynite structure of Harrison et al. (1998), Rietveld refinements of 10 of the reaction-reversal experiments gave an average unit-cell dimension for magnetite of a_0 = 8.377 ± 0.008 Å and for hercynite a_0 = 8.198 ± 0.005 Å. These values are similar to the unit-cell dimensions for the analyzed spinels given in Table 5, indicating relative uniformity in the composition of the spinels for the reaction-reversal experiments.

4 Discussion

4.1 Thermochemical modeling

Thermochemical modeling was done to allow extrapolation of the high-temperature results, where reaction rates are relatively fast, down to the lower-pressure and temperature conditions relevant to the near-surface conditions of Mars.

For the chemical system investigated in this study, namely Na_2O-FeO-Al_2O_3-SiO_2-H_2O-O_2, phase compositions can be plotted on the ternary diagram Al_2O_3-FeO-O_2 by projection from albite + quartz + H_2O, which is shown in Figure 8a. Figure 8b shows a Schreinemakers analysis of the invariant-point array of phases plotted in fO_2 vs

temperature space, where each reaction is uniquely labeled with the missing phase or phases in parentheses. The general orientation of this array can be determined by the degenerate (Smec, Alb, H_2O) reaction which is very similar to the fayalite-magnetite-quartz oxygen-buffering reaction 3 fayalite + O_2 = 2 magnetite + 3 quartz. The consistent appearance of magnetite + fayalite + quartz in the experiments of this study suggests that the upper-thermal stability of smectite is controlled by the (O_2) reaction:

$$1.0\ \text{Smec} = 0.23\ NaAlSi_3O_8\ (\text{Ab}) + 0.55\ Fe_2SiO_4\ (\text{Fay}) + 0.70\ FeAl_2O_4\ (\text{Herc}) + 1.58\ SiO_2\ (\text{Qtz}) + 0.25\ Fe_3O_4\ (\text{Mt}) + 1.0\ H_2O \quad (1)$$

where Smec has the composition $Na_{0.23}(Fe^{2+}_{2.05}Fe^{3+}_{0.50}Al_{0.45})(Al_{1.18}Si_{2.82})O_{10}(OH)_2$. This reaction, involving end-member phases in this chemically simplified system, is oxygen-conserving, making it independent of the oxygen fugacity. Reaction (1) involves the phases observed in this study and will be used to model the upper-thermal stability of smectite investigated here.

In reaction (1), the thermochemical properties of smectite are the least well defined. Therefore, extraction of the thermochemical data for smectite was done as follows. In the case of equilibrium at a given pressure (P) and temperature (T) one has:

$$\Delta G_{P,T} = 0 = \Delta H^o_{Po,To} - T\Delta S^o_{Po,To} + \int_{To}^{T} \Delta C_P dT - T\int_{To}^{T} \frac{\Delta C_P}{T} dT + \int_{Po}^{P} \Delta V^{solids} dP + RTlnK_a + RTln f^{P,T}_{H2O} \quad (2)$$

where $\Delta G_{P,T}$ is the Gibbs free energy of the reaction at the P and T of interest, $\Delta H^o_{Po,To}$ and $\Delta S^o_{Po,To}$ are the change in enthalpy and entropy of reaction, respectively, at the reference pressure (P_o) and temperature (T_o) conditions, ΔC_P is the heat capacity of the reaction, ΔV^{solids} is the volume change of the solids for the reaction, K_a the equilibrium

constant, and $f_{H2O}^{P,T}$ is the fugacity of water at the P and T of interest. The main thermochemical variables of interest are the enthalpy of formation (ΔH_f^o) and third-law entropy (S^o) for the smectite, as a reasonably well-constrained value for its volume is reported above and the heat capacity can be closely approximated by summation of component phases, particularly if those components are structurally related minerals (e.g., Helgeson et al., 1978, p. 60). Therefore, we can rearrange equation (2) to solve explicitly for $\Delta H_{Po,To}^o$ and $\Delta S_{Po,To}^o$ as a function of the remaining values collected into the single term G' with the expression:

$$-\Delta H_{Po,To}^o + T\Delta S_{Po,To}^o = G' = \int_{To}^{T} \Delta C_P dT - T\int_{To}^{T} \frac{\Delta C_P}{T} dT + \int_{Po}^{P} \Delta V^{solids} dP + RTlnK_a + RTlnf_{H2O}^{P,T} \quad (3)$$

Plotting G' as a function of T should yield a straight line with a slope of $\Delta S_{Po,To}^o$ and an intercept of $-\Delta H_{Po,To}^o$ of reaction. From these values, the ΔH_f^o and $S°$ of smectite can be calculated from the equations:

$$\Delta H_f^o(Smec) = -\Delta H_{Po,To}^o(reaction) + \sum \Delta H_f^o(products) \quad (4a)$$

$$S^o(Smec) = -\Delta S_{Po,To}^o(reaction) + \sum S^o(products) \quad (4b)$$

Thermochemical values for all of the phases except the smectite come from the database of Holland and Powell (2011). The heat capacity expression for smectite was estimated by a simple summation of sheet silicates according to the following equation:

Smectite = 0.23 Paragonite + 0.683 Ferro-talc + 0.5 Ferri-prehnite + 0.633 Margarite – 0.8167 Prehnite – 0.23 Pyrophyllite (5)

The four-term heat capacity expressions of each sheet silicate on the right side of equation (5) are reported in Holland and Powell (2011) and the resultant constants for

smectite are given in Table 6. Given the relatively low pressures (1-3 kbar) and temperatures (500-600°C) for the experiments in this study, the volume term in equation (3) was treated in the simplest of manners, which is to approximate the volumes of the solids as constants making the integral term equivalent to $\Delta V^{solids}(P-P_0)$. The validity of this simplification was checked by estimating the thermal expansion (α_o) and bulk modulus terms ($\kappa_0, \kappa_0', \kappa_0''$) for smectite as being those of ferro-talc and comparing the values of $\Delta V^{solids}(P-P_o)$ against the integrated-volume values from the Tait equation of state (TEOS) as used by Holland and Powell (2011), where it was found to amount to only a trivial difference (< 0.05 kJ). The fugacities of water at *P* and *T* are those from the equations of Pitzer and Sterner (1995) to allow extrapolation of the results obtained here at 1-3 kbar down to pressures of only 10's of bars and to be consistent with the Holland and Powell (2011) database. Finally, the activities of Fe_3O_4 and $FeAl_2O_4$ in the magnetite- and hercynite-rich spinels, respectively, were calculated from the compositions given in Table 5 using the AX62 program of Holland (2019), while all other phases have unit activity, which makes the equilibrium constant $K_a = (a_{FeAl2O4})^{0.7}(a_{Fe3O4})^{0.25}$.

Table 6 gives all of the data used in this study for smectite along with the derived values of ΔH_f^o (-5074.11 ± 0.84 kJ/mole) and *S*° (416.83 ± 0.98 J/K·mole) of smectite, where the uncertainties for the enthalpy and entropy are the standard errors of the intercept and slope, respectively, of the linear fit to the G' versus T plot. Figure 9 shows the experimental data from this study with the thermochemically-modeled reaction boundary. Extrapolation to higher pressures is not reliable because of the curvature of this boundary beyond the limits of the data; however, extrapolation to lower pressures,

where the reaction is primarily controlled by large changes in the properties of water, is more reliable and consistent with that of a typical dehydration reaction (e.g., Nordstrom and Munoz, 1985, Fig. 8-4).

4.2 Applications to Mars

Using these experimental data on the synthesis of Fe-rich tri-octahedral smectite over a range of bulk compositions, along with the thermochemical modeling of experiments defining the upper-thermal stability of a specific smectite, we will consider two applications of this work to Mars. In particular, we will consider the issues of (1) water storage on Mars, and (2) the high-temperature origins of smectite on Mars.

4.2.1 Water storage on Mars

The presence of an active hydrologic system involving substantial amounts of water early in the geological past of Mars is supported by various geomorphological (e.g., Carr and Head, 2003; Dickson et al. 2021) and isotopic studies (e.g., Kurokawa, et al., 2014; Villaneuva et al., 2015). Estimates of the amount of water needed to produce the geomorphic features on Mars, expressed in meters depth of a global equivalent layer of water (GEL), are typically in the range of 156-550 m and up to perhaps 1500 m GEL (Carr and Head, 2003; Di Achille and Hynek, 2010). The present-day inventory of H_2O occurring as sub-surface and polar ice (27-32 m GEL; Lasue et al., 2013; 2019; Mustard, 2019) coupled with estimates of water vapor loss from the atmosphere by photo-dissociation and solar-wind erosion throughout the geological history of Mars (4-25 m GEL; Jakosky et al., 2018) is insufficient to account for even the lower estimates of the original water volume (137 m GEL; Villaneuva et al., 2015), suggesting a sink that accounts for a minimum of ~80 m GEL. Scheller et al. (2021) recently modeled the

water inventory on Mars over time by including the processes of volcanic degassing, hydrogen escape from the atmosphere, and hydration of the Martian crust as potential controls on the hydrogen isotope changes on Mars. Their results pointed to the importance of crustal hydration as the possible missing reservoir. Therefore, this study can help shed light on the minimum depth (lower thermal limits) at which water can be stored in the crust of Mars as Mg-free, ferrous-iron rich tri-octahedral saponite (smectite).

Figure 10 shows the upper-thermal stability of ferrous-smectite determined in this study relative to the Noachian-period geotherm reported by Semprich et al. (2019). On the right side is the equivalent depth for Mars assuming an average density of 2.96 g/cm^3 for crustal rocks (Semprich et al., 2019) and an acceleration of gravity of 3.73 m/sec^2. The nearly vertical lines indicate the approximate location of the dehydration boundaries based on the data obtained here (Fig. 4) and the nearly isothermal nature of these boundaries determined by Carman (1974) for Na-phlogopite (aspidolite). These boundaries indicate the maximum water content held by smectite at a given depth, assuming it is at water saturation. Based on Figure 10, smectite is stable to a depth of about 30 km.

Phyllosilicate abundances ranging from 5-15 wt% have been observed in the Vera Rubin ridge (Rampe et al., 2020) and even up to 28 wt% in the mudstones of Murray formation, Gale Crater (Bristow et al., 2018), where tri-octahedral sheet silicates typically constitute 35-67% of those phyllosilicates. Using the lower value of 35%, the resultant tri-octahedral sheet silicate abundances is in the range of 1.8 – 10 wt%. If smectite is stable to 30 km depth, these abundances would equate to the storage of water amounting to 55 – 305 m GEL, well inside the range of the missing water content, and supports

earlier suggestions (e.g., Mustard, 2019) and the more recent conclusion of Scheller et al. (2021) that irreversible crustal hydration plays a key role in accounting for the missing water sink on Mars.

4.2.2 High-temperature origins of smectite on Mars

Ehlmann et al. (2013) identified seven formation mechanisms for making hydrated sheet silicates from a basaltic precursor. Four of these mechanisms were associated especially with Fe-Mg-smectites or saponite and involved high temperatures. These were (i) deep-seated metamorphism, (ii) hydrothermal alteration associated with volcanic activity (e.g., fumaroles and vents), (iii) hydrothermal activity from fluids exsolved during the final stages of magma crystallization, and (iv) hydrothermal activity from impacts. The present study can place some limits on the temperatures at which Fe-rich smectite could form by high-temperature mechanisms. Metamorphism by simple burial in a depositional environment along a Noachian geotherm of 20°C/km would give rise to Fe-smectite formation at temperatures up to 600°C at the maximum depth of 30 km (Fig. 10). This range of formation would readily account for smectite observed in the central uplifted regions, where material from depths of up to ~10 km could be exposed in craters that are ≈ 200 km diameter (Melosh, 1989, p. 78; Mustard, 2019).

The earlier study by Meunier et al. (2012) proposed that clay minerals may have formed on Mars during the Noachian period by magmatic precipitation. It is of interest, therefore, to see if the Fe-smectite of this study might be stable at the solidus temperatures of a water-saturated basalt. Although sought for, there was no clear indication that a silicate melt was produced at the highest temperatures of this study. Figure 11 compares the upper-thermal stability of Fe-smectite from this study with the

water-saturated solidus for tholeiitic basalt taken from Stern et al (1975). In this figure there is no overlap, even under water-saturated conditions, indicating that direct crystallization of Fe-smectite from a basalt is not likely. However, formation by hydrothermal activity associated with magma, either by circulation of water heated by intrusive rocks or from water exsolved during the final stages of solidification of intrusive rocks, is certainly possible starting at temperatures of approximately 600 °C or less.

A final model that will be considered here is that of Cannon et al. (2017) who proposed the formation of clay minerals on Mars during its earliest history from a super-critical atmosphere. In this model, clay minerals formed soon after accretion by the interaction of a hot and dense atmosphere of H_2O and CO_2, evolved originally from a cooling magma ocean, with the solidified crust. Cannon et al. (2017) did experiments over a range of pressure, temperature, and vapor composition conditions that demonstrated nucleation and growth of Fe-rich trioctahedral sheet silicates with basal reflections in the range of 10-14 Å, corresponding to 0-2 interlayers of water. The present study provides thermodynamic constraints on the equilibrium conditions of Fe-smectite formation at a water-vapor pressure of 100 bars, which is within the postulated range of pressures for a primordial atmosphere on Mars (Elkins-Tanton, 2008). Figure 12 shows the thermodynamically extrapolated results of this study (dashed curve) relative to the results of Cannon et al. (2017) (open circles) and to the liquid-vapor boundary for pure H_2O (solid curve). The calculated stability curve from this study lies above the liquid-vapor boundary indicating that formation from a vapor phase is certainly possible. At 100 bars, the calculated stability limit of Fe-smectite is 336 °C with an estimated

uncertainty of 25°C. The experiments done by Cannon et al. (2017) in the liquid (L) and supercritical (SC) regions are in agreement with this study; the sheet silicate formed in the vapor (V) region may either have formed metastably or may have sufficient Mg incorporated in its structure to stabilize it to higher temperatures. Overall, the potential for forming smectite by interaction between a primordial atmosphere and a basaltic crust is thermodynamically feasible below about 340 °C at pressures of about 100 bars.

5 Conclusions

This study investigated two main aspects of end-member Fe-rich (Mg-free) smectite with applications specifically to the stability of smectite on Mars. First, a range of bulk compositions along the join Fe-talc—Na-Fe-eastonite was prepared and treated at 500 °C and 2 kbar in the presence of 10 wt% H_2O and fO_2 near that of the fayalite-magnetite-quartz buffer. Each bulk composition yielded smectite, showing that Fe-rich smectite can form from a range of initial bulk compositions. Although perhaps coincidental, the bulk composition chosen for further investigation in this study (FTC87, Table 1) yielded smectite that is similar in composition to the average of Mars soil at Gale Crater (Berger et al., 2016) and a global basaltic regolith simulant (Cannon et al., 2019) (Figure 7), indicating it may be directly applicable to Mars. Second, the upper-thermal stability of the smectite formed from bulk composition FTC87 was determined over the range of 1-3 kbar and 530-640 °C at an fO_2 near that of the fayalite-magnetite-quartz buffer. Reactions were investigated using reaction-reversal mixtures consisting of equal proportions of the smectite-synthesis and smectite-breakdown products to minimize issues associated with nucleation kinetics. Reactions rates were found to be relatively quick at these conditions, such that a simple comparison of X-ray diffraction peak heights was sufficient to judge

the reaction direction. Four main conclusions were drawn from this experimentally determined stability curve:

1. Trioctahedral Fe-rich smectite with 0 interlayer water could be stable to a depth of 30 km and temperatures up to 600 °C assuming a linear geothermal gradient of 20 °C/km (Semprich et al., 2019), appropriate for the Noachian period presumably when much of the smectite on Mars formed. It should be noted that any Mg substitution for Fe will increase the thermal stability of smectite, potentially making 30 km a minimum depth of stability

2. Smectite, even with 0 interlayer water, has the potential to be a substantial reservoir for surface water based on the 3.8 wt% of water present as intralayer OH. A Martian crust with, for example, 1.8 wt% smectite to a depth of 30 km will store 55 m GEL of water, which is a substantial fraction of the minimum estimates of ~80 m GEL of missing water on Mars.

3. Even though trioctahedral Fe-smectite was found to have a fairly high thermal stability under water-saturated conditions, it does not appear that primary formation from a water-saturated basaltic melt on Mars is possible. However, formation by magma-induced hydrothermal processes at temperatures of, for example, 400 °C are possible at a depth of only 2 km.

4. Thermodynamic modeling of the upper-thermal stability of this Fe-smectite at 1-3 kbar allowed extrapolation of these results to lower pressures. At an atmospheric pressure of 100 bars, the maximum thermal stability of Fe-smectite forming from

a primordial atmosphere on Mars is possible at calculated temperatures up to ~340 °C.

Acknowledgements

Partial support for this study was provided by NSF grant EAR-1725053 to DMJ, which is gratefully acknowledged. We thank D. Collins for help with the electron microprobe analyses. The manuscript has greatly benefited from the reviews of J. Filiberto and an anonymous reviewer.

References

Baron, F., Petit, S., and Decarreau, A. (2019) Experimental evidence of the metastability of ferric smectite. Geochimica et Cosmochimica Acta, 265,69-84.

Basora, A.M., Jenkins, D.M., & Bish, D.L. (2012). The lower-pressure stability of glaucophane in the presence of paragonite and quartz in the system Na_2O-MgO-Al_2O_3-SiO_2-H_2O. American Mineralogist, 97, 713-726.

Berger, J.A., Schmidt, M. E., Gellert, R., Campbell, J. L., King, P. L., Flemming, R. L., Ming, D. W., Clark, B. C., Pradler, I., VanBommel, S. J. V., Minitti, M. E., Fairén, A. G., Boyd, N. I., Thompson, L. M., Perrett, G. M., Elliott, B. E., and Desouza, E. (2016) A global Mars dust composition refined by the alpha-particle X-ray spectrometer in Gale Crater. Geophysical Research Letters, 43, 67-75, doi:10.1002/2015GL066675.

Birle, J.D., Gibbs, G.V., Moore, P.B., & Smith, J.V. (1968). Crystal structures of natural olivines. American Mineralogist, 53, 807-824.

Bishop, J., Murad, E., Madejova, J., Komadel, P., Wagner, U., & Scheinost, A. (1999). Visible Mossbauer and infrared spectroscopy of dioctahedral smectites: Structural analyses of the Fe-bearing smectites Sampor, SWy-1 and SWa-1. In H. Komada,

A. Mermut, & J. Torrance (Eds.), Clay Minerals for Our Future. Proceedings of the 11th International Clay Conference (pp. 413-419).

Bristow, T. F., Rampe, E. B., Achilles, C. N., Blake, D. F., Chipera, S. J., Craig, P., et al. (2018). Clay mineral diversity and abundance in sedimentary rocks of Gale crater, Mars. Science Advances, 4(6): eaar3330, DOI: 10.1126/sciadv.aar3330.

Cannon, K., Parman, S. M., and Mustard, J. F. (2017). Primordial clays on Mars formed beneath a steam or supercritical atmosphere. Nature, 552, 88-91.

Cannon, K. M., Britt, D.T., Smith, T. M., Fritsche, R. F., and Batcheldor, D. (2019) Mars global simulant MGS-1: A Rocknest-based open standard for basaltic martian regolith simulants. Icarus, 317, 470-478.

Carman, J. H. (1974) Synthetic sodium phlogopite and its two hydrates: stabilities, properties, and mineralogic implications. American Mineralogist, 59, 261-273.

Carr, M. H., and Head, J. W., III, (2003) Oceans on Mars: An assessment of the observational evidence and possible fate. Journal of Geophysical Research: Planets, 108, NO. E5, 5042, doi:10.1029/2002JE001963

Carter, J., Loizeau, D., Mangold, N., Poulet, F., Bibring, J.-P., 2015. Widespread surface weathering on early Mars: a case for a warmer and wetter climate. Icarus 248, 373–382.

Chan, A., Jenkins, D. M., & Dyar, D. M. (2016). Partitioning of Chlorine Between NaCl Brines and Ferro-pargasite: Implications for the Formation of Chlorine- Rich Amphiboles in Mafic Rocks. The Canadian Mineralogist, 1-16.

Charpentier, D., Buatier, M., Jacquot, E., Gaudin, A., & Wheat, C. (2011). Conditions and mechanism for the formation of iron-rich Montmorillonite in deep sea

sediments (Costa Rica margin): Coupling high resolution mineralogical characterization and geochemical modeling. Geochimica et Cosmochimica Acta, 75, 1397-1410.

Chemtob, S.M., Nickerson, R. D., Morris, R. V., Agresti, D. G., and Catalano, J. G. (2015), Synthesis and structural characterization of ferrous trioctahedral smectites: Implications for clay mineral genesis and detectability on Mars, J. Geophys. Res.: Planets, 120, 1119–1140, doi:10.1002/2014JE004763.

Chemtob, S. M., Nickerson, R. D., Morris, V., Agresti, D. G., and Catalano, J. G. (2017) Oxidative alteration of ferrous smectites and implications for the redox evolution of early Mars. J. Geophys. Res.: Planets, 122, 2469–2488, doi: 10.1002/ 2017JE005331.

Chou, I-M. (1986) Permeability of precious metals to hydrogen at 2 kb total pressure and elevated temperatures. American Journal of Science, 286, 638-658.

Ciobanu, C. L., Verdugo-Ihl, M. R., Slattery, A., Cook, N.J., Ehrig, K., Courtney-Davies, L., and Wade, B. P. (2019) Silician magnetite: Si-Fe-nanoprecipitates and other mineral inclusions in magnetite from the Olympic Dam Deposit, South Australia. Minerals, 9, article 311, doi:10.3390/min9050311.

Curtin, D., & Smillie, G. (1981). Composition and origin of smectite in soils derived from basalt in Northern Ireland. Clays and Clay Minerals, 29, 277-284.

Decarreau, A. & Bonnin, D. (1986) Synthesis and crystallogenesis at low temperature of Fe(III)-smectites by evolution of coprecipitated gels: Experiments in partially reducing conditions. Clay Minerals, 21, 861-877.

Di Achille, G., and Hynek, B. M. (2010) Ancient ocean on Mars supported by global distribution of deltas and valleys. Nature Geoscience, 3, 459-463.

Dickson, J. L., Lamb, M. P., Williams, R. M. E., Hayden, A. T., and Fischer, W. W. (2021) The global distribution of depositional rivers on early Mars. Geology, 49, 504-509.

Driscall, J., Jenkins, D.M., Dyar, M.D., and Bozhilov, K.N. (2005) Cation ordering in synthetic low-calcium actinolite. American Mineralogist, 90, 900-911.

Ehlmann, B., Mustard, J., Murchie, S., Bibring, J., Meunier, A., Fraeman, A., & Langevin, Y. (2011). Subsurface water and clay mineral formation during the early history of Mars. Nature, 479, 53-60.

Ehlmann, B.L., Berger, G., Mangold, N., Michalski, J.R., Catling, D.C., Ruff, S.W., Chassefiere, E., Niles, P.B., Chavier, V., Poulet, F. (2013) Geochemical consequences of widespread clay mineral formation in Mars' ancient crust. Space Sci. Rev. 174, 329–364.

Elkins-Tanton, L.T., 2008. Linked magma ocean solidification and atmospheric growth for Earth and Mars. Earth Planet. Sci. Lett. 271, 181-191.

Ferrage, E. (2016) Investigation of the interlayer organization of water and ions in smectite from the combined use of diffraction experiments and molecular simulations. A review of methodology, applications, and perspectives. Clays and Clay Minerals, 64, 348-373.

Fox, V. K., Kupper, R. J., Ehlmann, B. L., Catalano, J. G., Razzell-Hollis, J., Abbey, W. J., Schild, D. J., Nickerson, R. D., Peters, J. C., Katz, S. M., and White, A. A. (2021) Synthesis and characterization of Fe(III)-Fe(II)-Mg-Al smectite solid

solutions and implications for planetary science. American Mineralogist, 106, 964-982.

Gaudin, A., Buatier, M., Beaufort, D., Petit, S., Grauby, O., & Decarreau, A. (2005). Characterization and origin of Fe 3+ -montmorillonite in deep-water calcareous sediments (Pacific Ocean, Costa Rica margin). Clays and Clay Minerals, 53, 452-465.

Giblin, L. E., Blackburn, W. H., and Jenkins, D. M. (1993) X-ray continuum discrimination technique for the energy dispersive analysis of fine particles. Analytical Chemistry, 65, 3576-3580.

Golla-Schindler, U., O'Neill, H.St.C., Putnis, A., 2005, Direct observation of spinodal decomposition in the magnetite-hercynite system by susceptibility measurements and transmission electron microscopy. American Mineralogist 90, 1278-1283.

Harder, H. (1978) Synthesis of iron layer silicate minerals under natural conditions. Clays and Clay Minerals, 26(1), 65-72.

Harrison, R. J., Redfern, S. A. T., and O'Neill, H. St. C. (1998) The temperature dependence of the cation distribution in synthetic hercynite ($FeAl_2O_4$) from in-situ neutron structure refinements. American Mineralogist, 83, 1092-1099.

Helgeson, H. C., Delany, J. M., Nesbitt, H. W. & Bird, D. K. (1978) Summary and critique of the thermodynamic properties of rock-forming minerals. American Journal of Science, 278A, 229 pp.

Holland, T. J. B. (2019) AX62, https://filedn.com/lU1GlyFhv3UuXg5E9dbnWFF/TJBHpages/ax.html

Holland, T. J. B, and Powell, R. (2011) An improved and extended internally consistent thermodynamic dataset for phases of petrological interest, involving a new equation of state for solids. Journal of Metamorphic Geology, 29, 333-383.

Jakosky, B. M., Brain, D., Chaffin, M., Curry, S., Deighan, J. et al. (2018) Loss of the Martian atmosphere to space: Present-day loss rates determined from *MAVEN* observations and integrated loss through time. Icarus, 315, 146-157.

Jenkins, D. M. (1987) Synthesis and characterization of tremolite in the system H_2O-CaO-MgO-SiO_2. American Mineralogist, 72, 707-715.

Jenkins, D. M. and Corona, J. C. (2006) The role of water in the synthesis of glaucophane. American Mineralogist, 91, 1055-1068.

Kloprogge, J., Komarneni, S., & Amonette, J. (1999). Synthesis of smectite clay minerals: A critical review. Clays and Clay Minerals, 47(9), 529-554.

Kurokawa, H., Sato, M., Ushioda, M., Matsuyama, T., Moriwaki, R., Dohm, J.M., and Usui, T. (2014) Evolution of water reservoirs on Mars: Constraints from hydrogen isotopes in martian meteorites. Earth and Planetary Science Letters, 394, 179-185.

Lasue, J., Mangold, N., Hauber, E., Clifford, S., Feldman, W., Gasnault, O., Brima, C., Maurice, S., and Mousis, O. (2013) Quantitative assessments of the martian hydrosphere. Space Science Reviews, 174, 155-212.

Lasue, J., Clifford, S. M., Conway, S. J., Mangold, N., and Butcher, F. E. G. (2019) The hydrology of Mars including a potential cryosphere, in, Filiberto, J., Schwenzer, S. P. (eds.) Volatiles in the Martian Crust. Elsevier, pp. 185-246.

Levien, L., Prewitt, C.T., & Weidner, D.J. (1980) Structure and elastic properties of quartz at pressure. American Mineralogist, 65, 920-930.

Melosh, H. J. (1989) Impact Cratering. Oxford University Press, New York, 245 pp.

Meunier, A., Petit, S., Ehlmann, B. L., Dudoignon, P., Westall, F., Mas, A., El Albani, A., and Ferrage, E. (2012) Magmatic precipitation as a possible origin of Noachian clays on Mars. Nature Geoscience, 5, 739-743.

Michalski, J., Cuadros, J., Bishop, J., Dyar, M., Dekov, V., & Saverio, F. (2015). Constraints on the crystal-chemistry of Fe/Mg-rich smectitic clays on Mars and links to global alteration trends. Earth and Planetary Science Letters, 427, 215-225.

Milliken, R., & Bish, D. (2010). Sources and sinks of clay minerals on Mars. Philosophical Magazine, 90(17-18), 2293-2308.

Moore, D. M., and Reynolds, R. C., Jr. (1997) X-ray Diffraction and the Identification and Analysis of Clay Minerals. Oxford University Press, Oxford, UK, 378 pp.

Mücke, A. (2003) Fayalite, pyroxene, amphibole, annite and their decay products in mafic clots within Younger Granites of Nigeria: Petrography, mineral chemistry and genetic implications. Journal of African Earth Sciences, 36, 55-71.

Mustard, J. R. (2019) Sequestration of volatiles in the Martian crust through hydrated minerals: A significant planetary reservoir of water, in, Filiberto, J., Schwenzer, S. P. (eds.) Volatiles in the Martian Crust. Elsevier, pp. 247-263.

Nordstrom, D. K., and Munoz, J. L. (1985) Geochemical Thermodynamics. Benjamin/Cummings Publishing Co., Menlo Park, CA, USA. 477 pp.

Nguyen-Thanh, L., Hoang-Minh, T., Kasbohm, J., Herbert, H., Thuy, D., & Thi, L. (2014). Characterization of Fe-smectites and their alteration potential in relation to engineered barriers for HLW repositories: The Nui Nua clay, Thanh Hoa Province, Vietnam. Applied Clay Science, 101, 168-176.

Peretyazhko, T., Niles, P., Sutter, B., Morris, R., Agresti, D., Le, L., & Ming, D. (2018). Smectite formation in the presence of sulfuric acid: Implications for acidic smectite formation on early Mars. Geochimica et Cosmochimica Acta, 220, 248-260.

Pitzer, K. S., and Sterner, S. M. (1995) Equations of state valid continuously from zero to extreme pressures with H_2O and CO_2 as examples. International Journal of Thermophysics, 16, 511-518.

Poulet, F., J.-P. Bibring, J. F. Mustard, A. Gendrin, N. Mangold, Y. Langevin, R. E. Arvidson, B. Gondet, & C. Gomez (2005), Phyllosilicates on Mars and implications for early Martian climate, Nature, 438, 623 – 627.

Rampe, E. B., Bristow, T. F., Morris, R. V., Morrison, S. M., Achilles, C. N., Ming, D. W., Vaniman, D. T., Blake, D. F., Tu, V. M., Chipera, S. J., Yen, A. S., Pertyashko, T. S., Downs, R. T., Hazen, R. M., Treiman, A. H., Grotzinger, J. P., Castle, N., Craig, P. I., Des Marais, D. J., Thorpe, M. T., Walroth, R. C., Downs, G. W., Fraeman, A. A., Siebach, K. L., Gellert, R., Lafuente, B., McAdam, A. C., Meslin, P.-Y., Sutter, B., and Salvatore, M. R. (2020) Mineralogy of Vera Rubin ridge from the Mars Science Laboratory CheMin instrument. Journal of Geophysical Research: Planets, 125, e2019JE006306, 31 p.

Reed, S. J. B. (1996) Electron Microprobe Analysis and Scanning Electron Microscopy in Geology. Cambridge University Press.

Righter, K., Herd, C. D. K., and Boujibar, A. (2020) Redox processes in early Earth accretion and in terrestrial bodies. Elements, 16(3), 161-166, doi: 10.2138/gselements.16.3.161.

Scheller, E. L., Ehlmann, B. L., Hu, R., Adams, D. J., and Yung, Y. L. (2021) Long-term drying of Mars by sequestration of ocean-scale volumes of water in the crust. Science, 372(6537), 56-62.

Semprich, J., Schwenzer, S. P., Treiman, A. H., and Filiberto, J. (2019) Phase equilibria modeling of low-grade metamorphic Martian rocks. Journal of Geophysical Research: Planets, 124, 681-702.

Slade, P.G., Stone, P.A., Radoslovich, E.W., 1985, Interlayer structures of the two-layer hydrates of Na- and Ca-vermiculites. Clays and Clay Minerals 33, 51-61.

Srodon, J. (1980). Precise identification of illite/smectite interstratifications by x-ray powder diffraction. Clays and Clay Minerals, 28(6), 401-411.

Stern, C. R., Huang, W-L., and Wyllie, P. J. (1975) Basalt-andesite-rholite-H_2O: crystallization intervals with excess H_2O and H_2O-undersaturated liquidus surfaces to 35 kilobars, with implications for magma genesis. Earth and Planetary Science Letters, 28, 189-196.

Szczerba, M., and Ufer, K. (2018) New model of ethylene glycol intercalate in smectites for XRD modelling. Applied Clay Science, 153, 113-123.

Toby, B. H., and Von Dreele, R. B. (2013). GSAS-II: the genesis of a modern open-source all purpose crystallography software package. Journal of Applied Crystallography, 46(2), 544-549.

Treiman, A. H., Morris, R. V., Agresti, D. G., Graff, T. G., Achilles, C. H., Rampe, E. B., Bristow, T. F., Ming, D. W., Blake, D. F. Vaniman, D. T., Bish, D. L., Chipera, S. J., Morrison, S. M., and Downs, R. T. (2014) Ferrian saponite from the Santa Monica Mountains (California, U.S.A., Earth): Characterization as an analog for clay minerals on Mars with application to Yellowknife Bay in Gale Crater. American Mineralogist, 99, 2234-2250.

Tuff, J., Wade, J., and Wood, B. J. (2013) Volcanism on Mars controlled by early oxidation of the upper mantle. Nature, 498, 342-345.

Turnock, A.C., Eugster, H.P., 1962, Fe-Al oxides: Phase relationships below 1,000 °C. J. Petrol. 3, 533-565.

Vaniman, D. T., Bish, D. L., Ming, D. W., Bristow, T. F, Morris, R.V., Blake, D. F., Chipera, S. J., Morrison, S. M., Treiman, A. H., Rampe, E. G., Rice, M., Achilles, C. N., Grotzinger, J. P., McLennan, S. M.,Williams, J., Bell, J. F. III, Newsom, H. E., Downs, R. T., Maurice, S., Sarrazine, P., Yen, A. S., Morookian, J. G., Farmer, J. D., Stack, K., Milliken, R. E., Ehlmann, B. L. Ehlmann, Sumner, D. Y., Berger, G., Crisp, J. A., Hurowitz, J. A., Anderson, R., Des Marais, D. J.,Stolper, E. M., Edget, K. S., Gupta, S., Spanovich, N. (2014) Mineralogy of a mudstone at Yellowknife Bay, Gale Crater, Mars. Science, 343(6169), https://doi.org/10.1126/science.1243480, 1243480.

Villaneuva, G. L., Mumma, M. J., Novak, R. T., Käufl, H. U., Hartogh, P., Encrenaz, T., Tokunaga, A., Khayat, A., and Smith, M. D. (2015) Strong water isotopic anomalies in the martian atmosphere: Probing current and ancient reservoirs. Science, 348, 218-221.

Wechsler, B.A., Lindsley, D.H., & Prewitt, C.T. (1984) Crystal structure and cation distribution in titanomagnetites (Fe3–xTixO4). American Mineralogist, 69, 754–770.

Table 1. Bulk compositions investigated in the synthesis of smectite.

Sample	Bulk Composition
Smec1	$Na(Fe_3)(AlSi_3)O_{10}(OH)_2$
Smec2	$Na_{0.4}(Fe_{1.8}Al_{0.8}\square_{0.4})(Al_{0.4}Si_{3.6})O_{10}(OH)_2$
FTC69	$Na_{0.3}(Fe_{2.4}Al_{0.6})(AlSi_3)O_{10}(OH)_2$
FTC75	$Na_{0.3}(Fe_{2.5}Al_{0.5})(Al_{0.75}Si_{3.25})O_{10}(OH)_2$
FTC81	$Na_{0.2}(Fe_{2.6}Al_{0.4})(Al_{0.6}Si_{3.4})O_{10}(OH)_2$
FTC87	$Na_{0.1}(Fe_{2.7}Al_{0.3})(Al_{0.4}Si_{3.6})O_{10}(OH)_2$
FTC91	$Na_{0.1}(Fe_{2.8}Al_{0.2})(Al_{0.3}Si_{3.7})O_{10}(OH)_2$

Table 2. Conditions and products of smectite synthesis and breakdown experiments, arranged in order of increasing temperature.

Sample ID	P (kbar)	T (°C)	t (h)	Products and comments
Smec1-2	2	500	120	alb, mt, smec, fay
Smec1-3	2	500	336	alb, mt, smec, fay, qtz
Smec2-1	2	500	312	qtz, mt, smec, alb, berth
FTC69-1	2	500	168	qtz, mt, smec
FTC75-1	2	500	240	qtz, mt, smec
FTC81-1	2	500	240	qtz, cri, mt, smec
FTC87-1	2	500	168	qtz, mt, smec
FTC87-4	2	500	72	qtz, mt, smec
FTC87-5	2	500	144	qtz, mt, fay, smec
FTC91-1	2	500	168	qtz, fay, mt, smec; capsule ruptured
FTC91-2	2	500	168	qtz, mt, fay, smec
FTC87-7	2	520	144	qtz, mt, fay, smec
Smec1-1	2	700	168	qtz, mt, fay
FTC87-2	2	700	168	qtz, fay, ab, herc
FTC87-3	2	700	72	fay, qtz, herc
FTC87-6	2	700	144	fay, qtz, hrc

Abbreviations: alb = albite, berth = berthierine, cri = cristobalite, fay = fayalite, herc = hercynite, mt = magnetite, qtz = quartz, smec = smectite

Table 3. Electron microprobe analysis of smectite from selected samples. Analyses are the average of *n* analyses, with uncertainties (1σ) in last digit given in parentheses.

Sample	Smec1-3	Smec2-1	FTC87-1	FTC87R-3	FTC87R-4	FTC87R-8	Average[b]
n	7	9	10	13	9	6	38
SiO_2	34.7(29)	30.5(29)	31.4(23)	29.0(25)	27.8(28)	28.1(50)	29.2(32)
Al_2O_3	13.8(8)	16.6(24)	15.5(21)	13.8(25)	13.4(25)	15.0(32)	14.3(26)
FeO	34.7(28)	32.3(26)	32.0(16)	31.8(22)	30.8(13)	30.9(30)	31.5(20)
Na_2O	5.7(9)	1.3(7)	1.7(7)	1.1(5)	1.2(4)	0.87(33)	1.2(6))
Total	89.0(39)	80.8(55)	80.7(39)	75.7(54)	73.2(54)	74.8(70)	76.3(58)
Si	2.96(11)	2.78(21)	2.88(19)	2.82(12)	2.80(9)	2.68(34)	2.82(18)
^{IV}Al	1.04(11)	1.22(21)	1.12(19)	1.18(12)	1.18(9)	1.32(34)	1.18(18)
∑ tet	4.00	4.00	4.00	4.00	3.98(6)	4.00	4.00
^{VI}Al	0.36(12)	0.55(15)	0.54(6)	0.40(20)	0.39(22)	0.44(15)	0.45(18)
Fe^{2+}	2.45(21)	2.01(24)	2.18(25)	2.02(15)	1.98(26)	1.86(35)	2.05(25)
$^{a}Fe^{3+}$	0.04(10)	0.45(35)	0.27(28)	0.58(29)	0.63(48)	0.70(39)	0.50(37)
∑ oct	2.85(14)	3.00	2.99(1)	3.00	3.00	3.00	3.00
Na	0.94(12)	0.23(12)	0.31(13)	0.20(9)	0.23(7)	0.18(9)	0.23(11)
∑ cations	7.79(7)	7.23(12)	7.31(12)	7.20(9)	7.21(10)	7.18(9)	7.23(11)

[a] Ferric iron calculated by summing the octahedral cations to 3.0.

[b] Average smectite composition of FTC87-1, FTC87R-3, FTC87R-4, and FTC87R-8.

Table 4: Experimental conditions and products of reversal experiments.

Sample code[a]	P (kbar)	T (°C)	t (h)	Products and comments[b]
FTC87R-8	1.0	530	168	qtz, fay, smec, mt; smec growth
FTC87R-7	1.0	545	144	qtz, mt, fay, herc; smec breakdown
FTC87R-6	1.0	570	48	qtz, mt, fay, ab, herc
FTC87R-5	1.0	580	120	qtz, mt, fay, ab, herc
FTC87R-2	2.0	550	168	qtz, mt, fay, smec, herc
FTC87R-4	2.0	560	48	qtz, fay, mt, smec, herc
FTC87R-3	2.0	580	48	qtz, fay, mt, herc; smec growth
FTC87R4-1	2.0	600	168	qtz, fay, ab, mt, herc; smec breakdown
FTC87R-1	2.0	650	120	qtz, fay, herc
FTC87R2-2	2.74	600	192	qtz, fay, mt, smec, herc; pressure drop; smec growth
FTC87R-11	2.8	620	48	qtz, fay, ab, mt, herc; quenched early due to pressure drop; smec breakdown
FTC87R2-3	3.0	580	144	qtz, fay, mt, smec, herc, parag (trace)
FTC87R-9	3.0	600	168	qtz, mt, smec, herc; f_{O2} high; smec growth
FTC87R-10	3.0	640	168	qtz, fay, herc, ab
FTC87R2-4	3.1	620	168	qtz, fay, ab, herc, mt; f_{O2} low; smec breakdown

[a]Starting mixtures used for these experiments were as follows: FTC87R-x and FTC87R2-x consisted of equal mixtures of FTC87-1 and FTC87-2 (Table 2), while FTC87R4-x consisted of equal mixtures of FTC87-5 and FTC87-6 (Table 2).

[b]Abbreviations: chl = chlorite, parag = paragonite; others as in Table 2

Table 5. Compositions, proportions and activities of spinel components, and unit-cell dimensions of magnetite and hercynite from select reaction-reversal experiments. Uncertainties (1σ) in last digit given in parentheses.

Sample	FTC87R-3	FTC87R-4	FTC87R-8	FTC87R-5	FTC87R-5	FTC87R-10
Phase	Mt	Mt	Mt	Mt	Herc	Herc
n	10	8	11	4	3	10
SiO_2	1.89(42)	2.02(87)	1.79(60)	2.18(74)	2.11(62)	2.70(12)
Al_2O_3	2.69(69)	2.06(72)	1.08(34)	3.74(73)	39(13)	44.5(35)
FeO	79.1(39)	79.5(61)	84.2(35)	85.0(23)	53.8(78)	43.8(27)
Na_2O	0.09(7)	0.08(7)	0.05(4)	0.04(3)	0.18(14)	0.16(30)
Total	83.8(33)	83.6(55)	87.1(32)	90.9(18)	95.6(45)	91.2(51)
Cations*						
Si	0.08(2)	0.08(4)	0.07(2)	0.08(3)	0.07(2)	0.09(4)
Al	0.13(3)	0.10(4)	0.05(2)	0.17(4)	1.47(37)	1.71(7)
Fe^{2+}	1.08(2)	1.08(4)	1.07(2)	1.08(3)	1.07(2)	1.09(4)
Fe^{3+}	1.70(6)	1.72(10)	1.80(6)	1.66(8)	0.39(32)	0.11(7)
∑ cations	3.00	3.00	3.00	3.00	3.00	3.00
Proportions of spinel components						
X_{Ahren}	0.08	0.08	0.07	0.08	0.07	0.09
X_{Herc}	0.07	0.05	0.03	0.09	0.74	0.86
X_{Mt}	0.85	0.87	0.90	0.83	0.20	0.05
activities**						
a_{Herc}	0.12	0.08	0.02	0.16	0.69	0.81
a_{Mt}	0.86	0.88	0.91	0.85	0.69	0.17
Unit-cell dimension						
a_0 (Å)	8.3799(8)	8.380(1)	8.384(1)	8.362(1)	8.194(2)	8.186(1)

*Cations normalized to 4 oxygens and Fe^{3+} calculated as discussed in the text. Ahren = ahrensite (Fe_2SiO_4)

** Activities for hercynite (a_{Herc}) and magnetite (a_{Mt}) calculated at 2 kbar and 600°C using the program AX62 of Holland (2019)

Table 6. Thermochemical data at 1 bar and 298 K derived for smectite in this study

ΔH_f^o (kJ/mole)	$S°$ (J/K·mole)	V^o (kJ/kbar)	C_P (kJ/K·mole)*			
			a	*b*	*c*	*d*
-5074.11 ± 0.80	416.83 ± 0.93	15.27 ± 0.09	0.6479	2.1873×10^{-5}	-5259.7	-4.3379

*Constants for the heat-capacity expression: $C_P = a + b(T) + cT^{-2} + dT^{-1/2}$, with the resultant values being in kJ/K·mol.

Figure Captions

Figure 1. Compositions of terrestrial and synthetic Fe-rich smectite reported in the literature shown as the atomic proportions (mol%) of Al-(Na+Ca+K)-Fe_{total}. The dashed line represents the join between ideal Na-Fe-eastonite and Fe-talc plotted here for reference. Samples listed: FX21-K, L, M, N, O from Fox et al. (2021), NT14-MC (My Cai clay), CD (Co Dinh clay) from Nguyen-Thanh et al. (2014), and MU03-N10, N18, N26 from Mücke (2003).

Figure 2. Bulk compositions for smectite synthesis investigated in this study. Dashed line indicates the join between the end-members Na-Fe-eastonite and Fe-Talc.

Figure 3. Back-scattered electron image of Smec2-1 showing the characteristic sheet morphology (in cross section) of smectite (Smec) along with darker-grey quartz (Qtz) and small brighter grains of magnetite (Mt).

Figure 4. X-ray diffraction patterns for smectite made from the same bulk composition (FTC87, Table 1) showing the location of the (001) diffraction maximum at room temperature (RT) as well as elevated temperatures (indicated). The two top patterns were obtained at different times of the year, where the top pattern was obtained during late spring with high relative humidity (RH, ~ 50%) in the lab with smectite in its bi-hydrated form (2L), while the second pattern was obtained in late fall when the RH was lower (~30%) with smectite in its mono-hydrated form (1L). Smectite with no interlayer water (0L) occurs between 100 and 150 °C.

Figure 5. Experimental results on the upper-thermal stability of iron smectite formed from bulk composition FTC87 (Table 1). Solid circles indicate growth while open circles indicate breakdown of smectite. Boundary shown is simply fit by eye.

Figure 6. Representative XRD patterns demonstrating the growth (A), starting mixture (B), and breakdown (C) of smectite at 1 kbar and the temperatures shown. Intensities of all patterns are scaled to match the strongest quartz peak, and some of the stronger peaks are labeled with the corresponding phases. Smec (1L) and Smec (2L) indicate smectite with 1 and 2 water interlayers, respectively, with the remaining abbreviations as in Table 2.

Figure 7. Electron microprobe analysis of the smectite used in the starting material (solid circle) and of the smectite formed in several smectite-growth reaction reversals (open circles). The bulk composition of the smectite starting mixture (FTC87) is shown for reference (crossed circle), along with an average bulk composition of Gale Crater soil (open star; Berger et al., 2016) and the MGS-1 Mars regolith simulant (solid star; Cannon et al., 2019).

Figure 8. (a) Compositions of the phases encountered in this study as shown projected from albite + H_2O + SiO_2 onto the ternary plane Al_2O_3-O_2-FeO. (b) Schreinemakers analysis of the chemographic relations in (a) plotted in fO_2 vs temperature space. Univariant reactions are labeled with the phase that is absent in the univariant reaction assemblage. Reaction (1) in the text is the (O_2) reaction.

Figure 9. Upper-thermal stability curve of iron smectite modeled with a thermochemical fit to the experimental data according to reaction (1) in the text. Extrapolated portions of this curve are shown as dashed lines.

Figure 10. Upper-thermal stability of Fe-smectite relative to an estimated 20°C/km geothermal gradient for the Noachian era on Mars. Intersection of this geotherm with the stability boundary defines the maximum pressure (depth) at which tri-octahedral

iron-rich smectite could be stable. Nearly vertical lines at lower temperatures indicate the approximate dehydration boundaries for smectite with 2- and 1-interlayer H_2O. Maximum water contents (wt%) of the smectite are indicated at the dehydration depths along the geotherm.

Figure 11. Comparison of the upper-thermal stability of the Fe-smectite from this study to the water-saturated solidus of a tholeiitic basalt reported by Stern et al. (1975).

Figure 12. Upper-thermal stability of the Fe-smectite of this study (dashed curve) extrapolated to the low water-vapor pressures relevant to smectite formation from a dense primordial atmosphere on Mars. Liquid-vapor boundary for H_2O is shown for comparison. Estimated uncertainty (unc.) for the location of this boundary is shown by the error bracket. Open circles are data from Cannon et al. (2017, C17) on the synthesis of sheet silicates in the liquid (L), supercritical (SC), and vapor (V) regions of H_2O.

Figure 1.

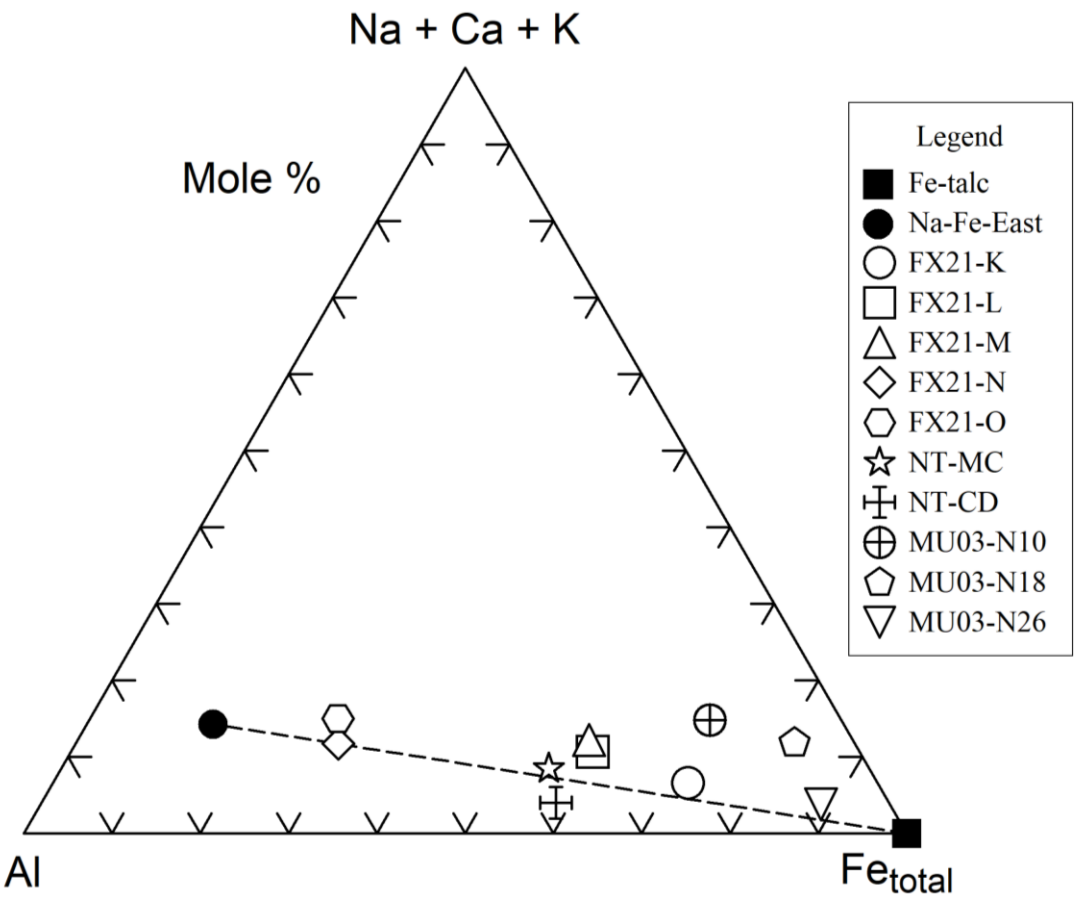
Na + Ca + K
Mole %
Legend
Fe-talc
Na-Fe-East
FX21-K
FX21-L
FX21-M
FX21-N
FX21-O
NT-MC
NT-CD
MU03-N10
MU03-N18
MU03-N26
Al
Fe$_{total}$

Figure 2

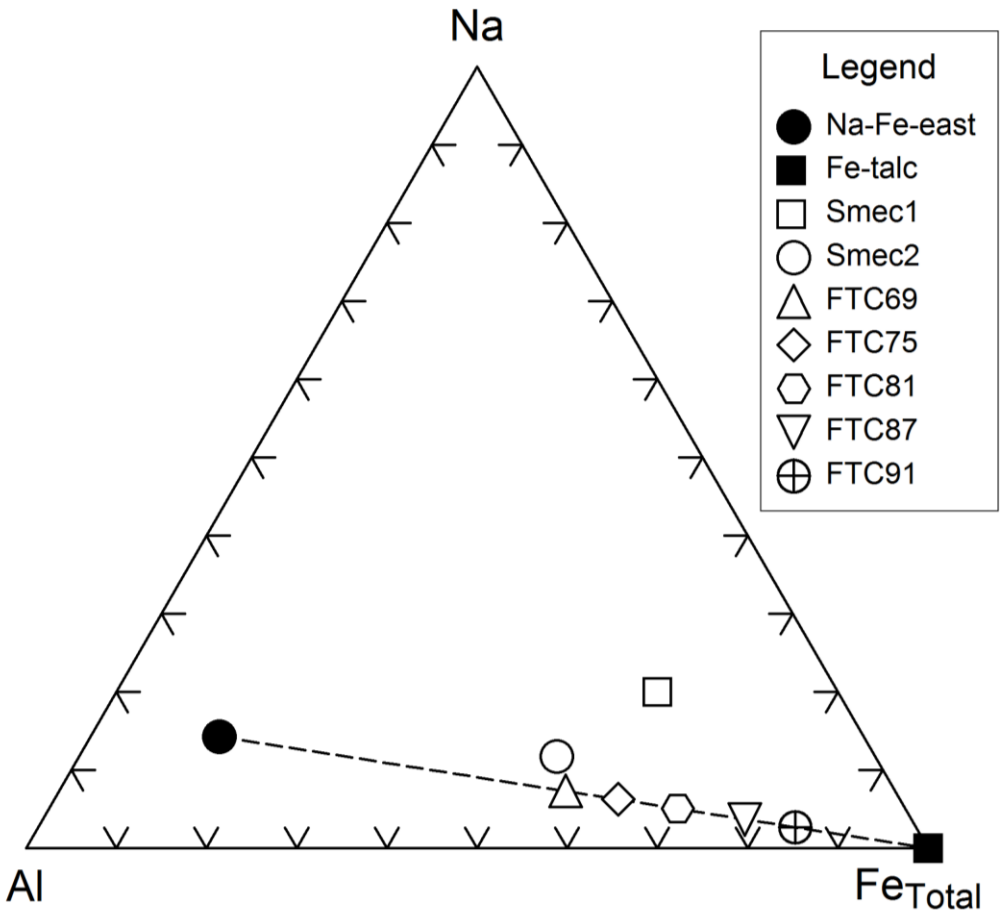
Na
Legend
Na-Fe-east
Fe-talc
Smec1
Smec2
FTC69
FTC75
FTC81
FTC87
FTC91
Al
Fe$_{Total}$

Figure 3

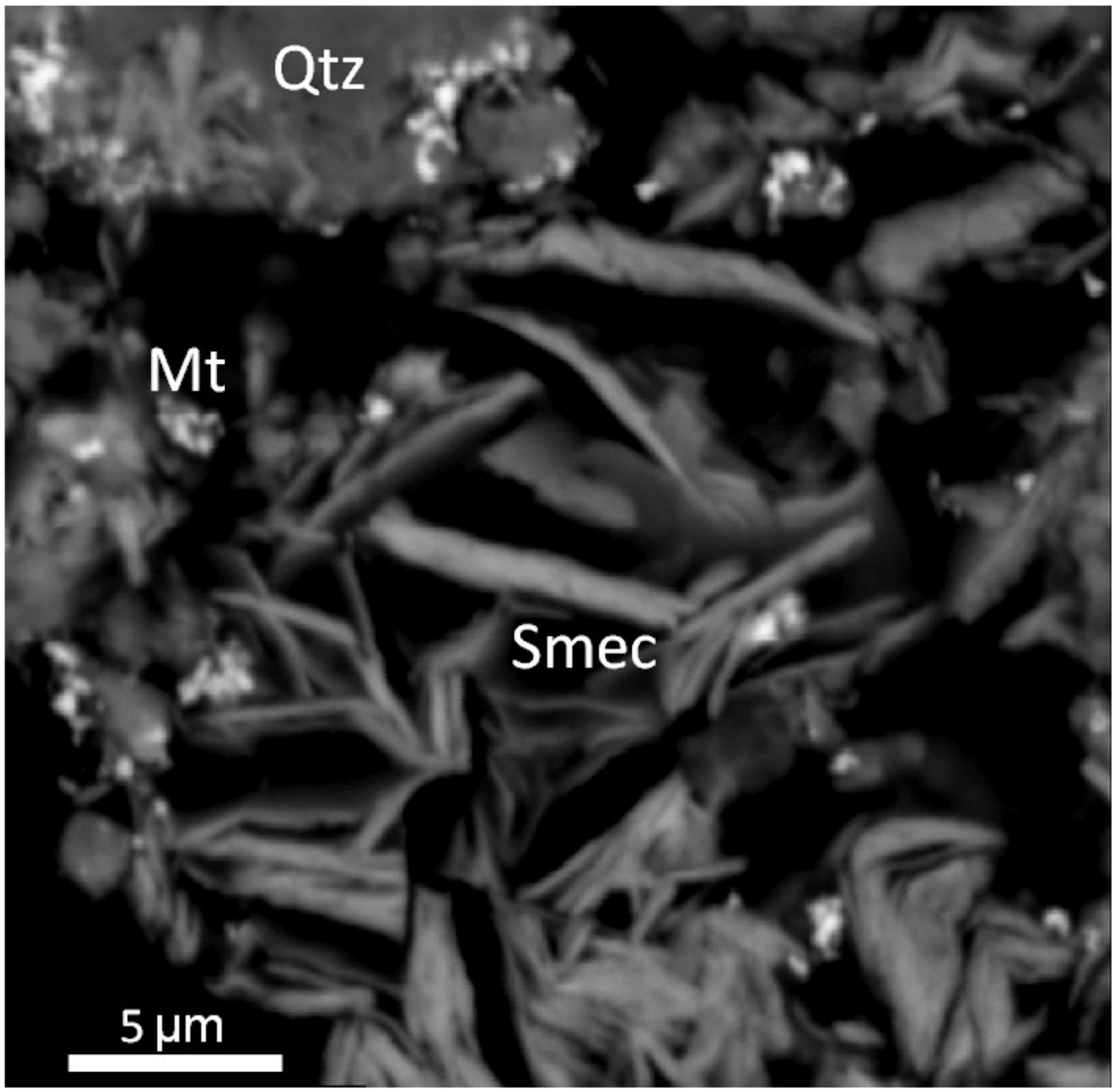

Figure 4

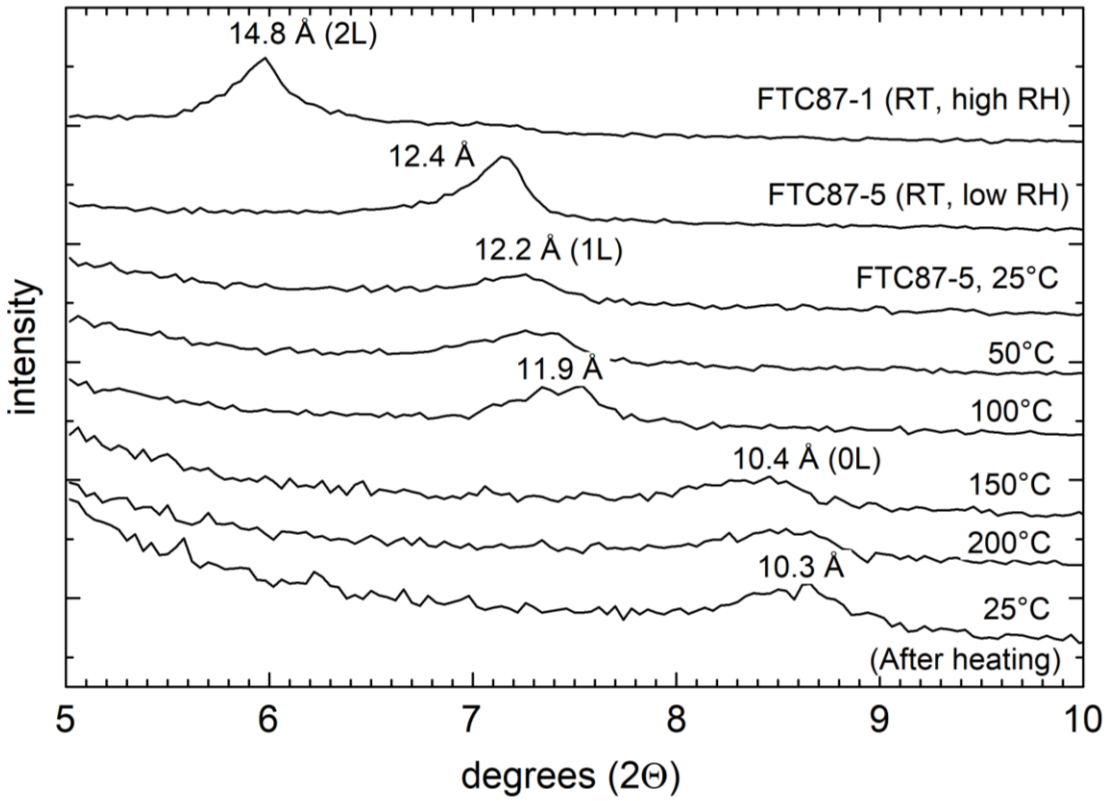
14.8 Å (2L)
FTC87-1 (RT, high RH)
12.4 Å
FTC87-5 (RT, low RH)
12.2 Å (1L)
FTC87-5, 25°C
50°C
11.9 Å
100°C
10.4 Å (0L)
150°C
200°C
10.3 Å
25°C
(After heating)
intensity
5
6
7
8
9
10
degrees (2Θ)

Figure 5

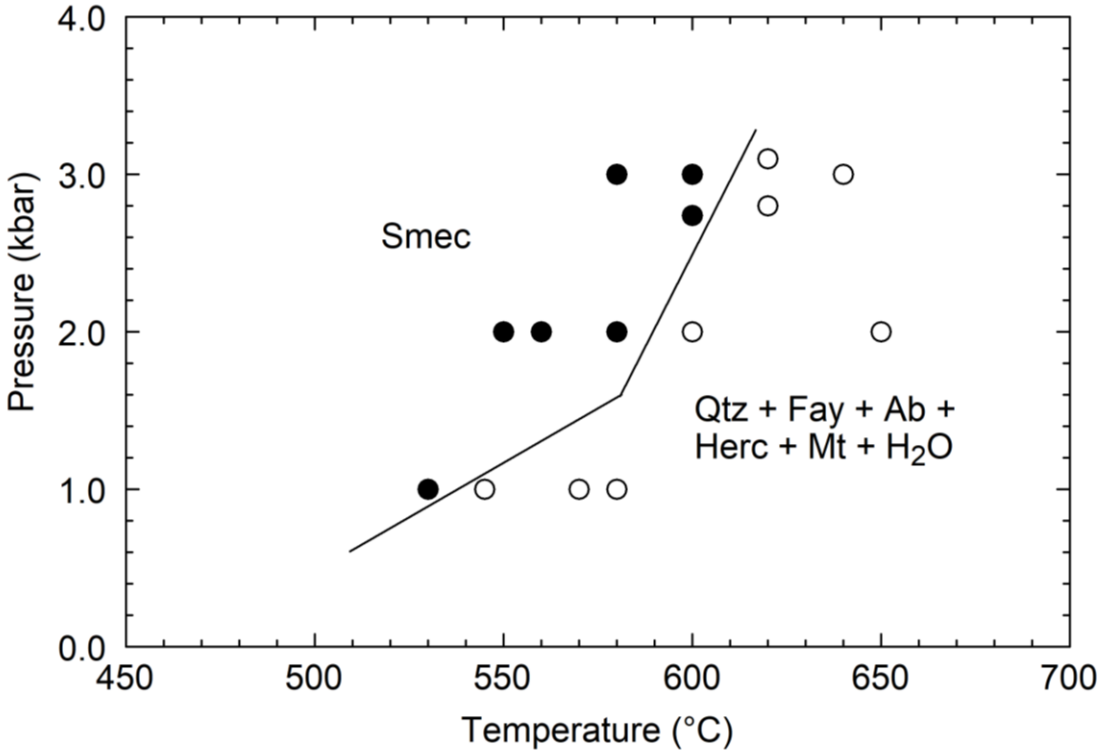
4.0
3.0
2.0
1.0
0.0
Pressure (kbar)
450
500
550
600
650
700
Temperature (°C)
Smec
Qtz + Fay + Ab +
Herc + Mt + H_2O

Figure 6

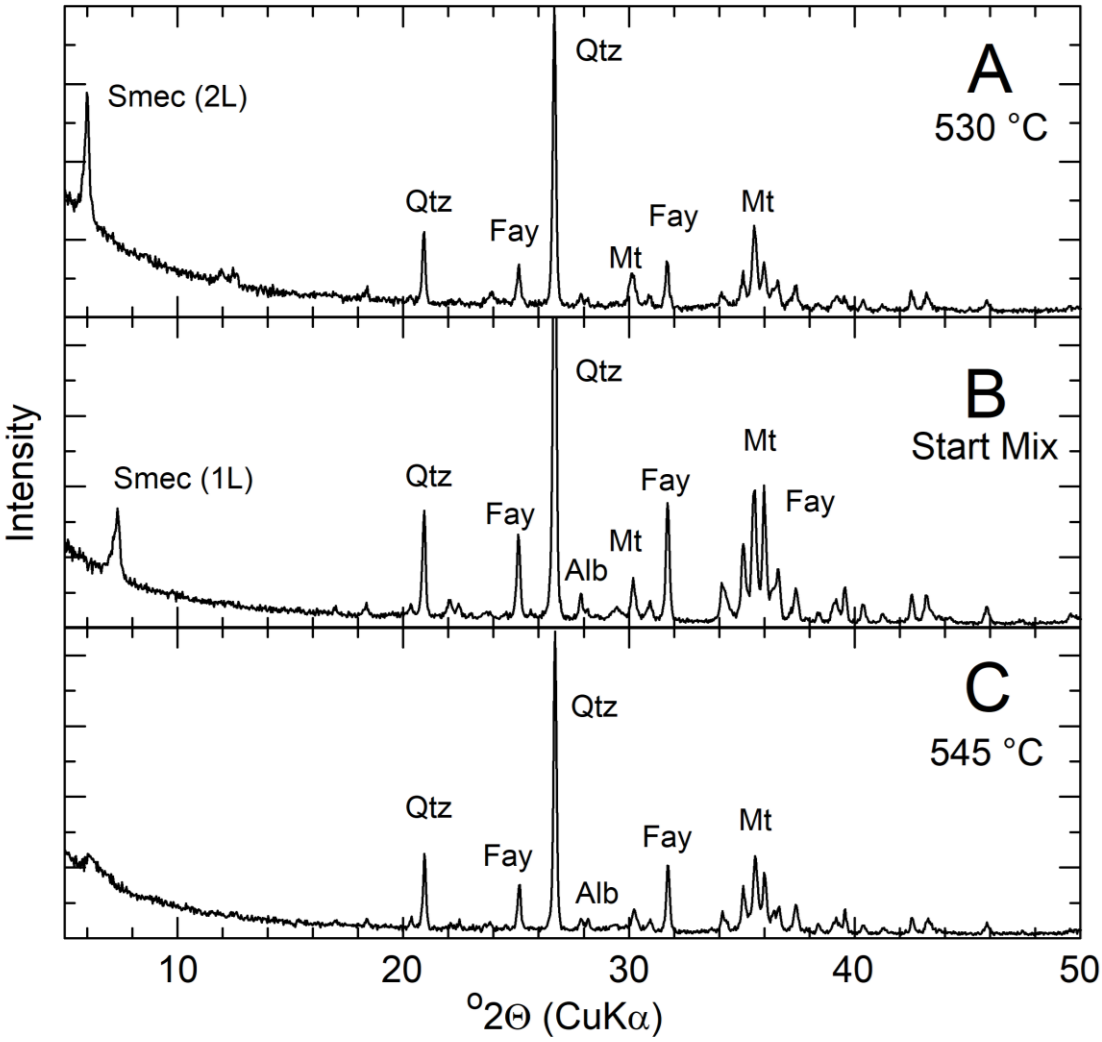
A
530 °C
Smec (2L)
Qtz
Qtz
Fay
Mt
Fay
Mt
B
Start Mix
Smec (1L)
Qtz
Qtz
Fay
Alb
Mt
Fay
Mt
Fay
C
545 °C
Qtz
Qtz
Fay
Alb
Fay
Mt
Intensity
10
20
30
40
50
°2Θ (CuKα)

Figure 7

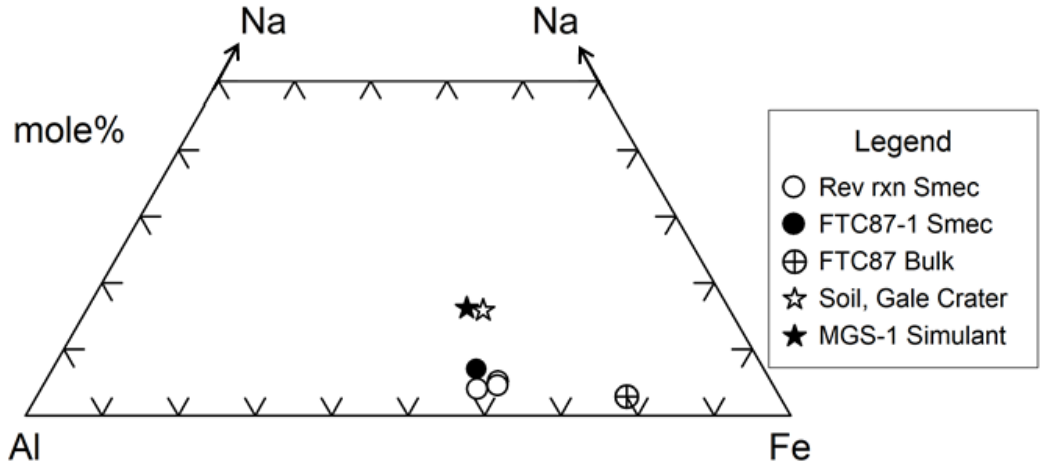
Na
Na
mole%
Al
Fe
Legend
Rev rxn Smec
FTC87-1 Smec
FTC87 Bulk
Soil, Gale Crater
MGS-1 Simulant

Figure 8

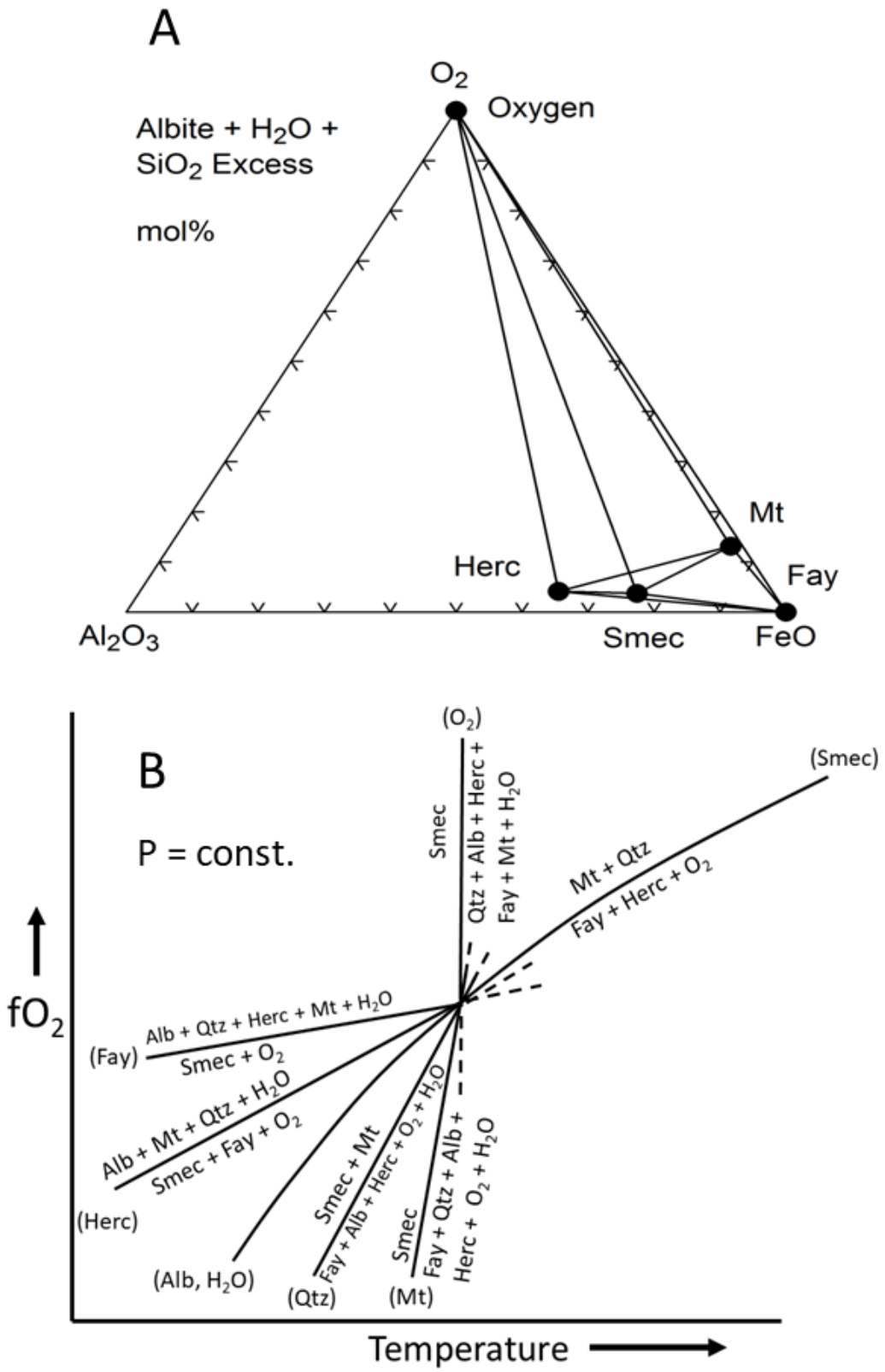
A
O_2
Oxygen
Albite + H_2O +
SiO_2 Excess
mol%
Mt
Herc
Fay
Al_2O_3
Smec
FeO
B
P = const.
(O_2)
(Smec)
Smec
Qtz + Alb + Herc +
Fay + Mt + H_2O
Mt + Qtz
Fay + Herc + O_2
fO_2
Alb + Qtz + Herc + Mt + H_2O
(Fay)
Smec + O_2
Alb + Mt + Qtz + H_2O
Smec + Fay + O_2
(Herc)
Smec + Mt
Fay + Alb + Herc + O_2 + H_2O
Smec
Fay + Qtz + Alb +
Herc + O_2 + H_2O
(Alb, H_2O)
(Qtz)
(Mt)
Temperature

Figure 9

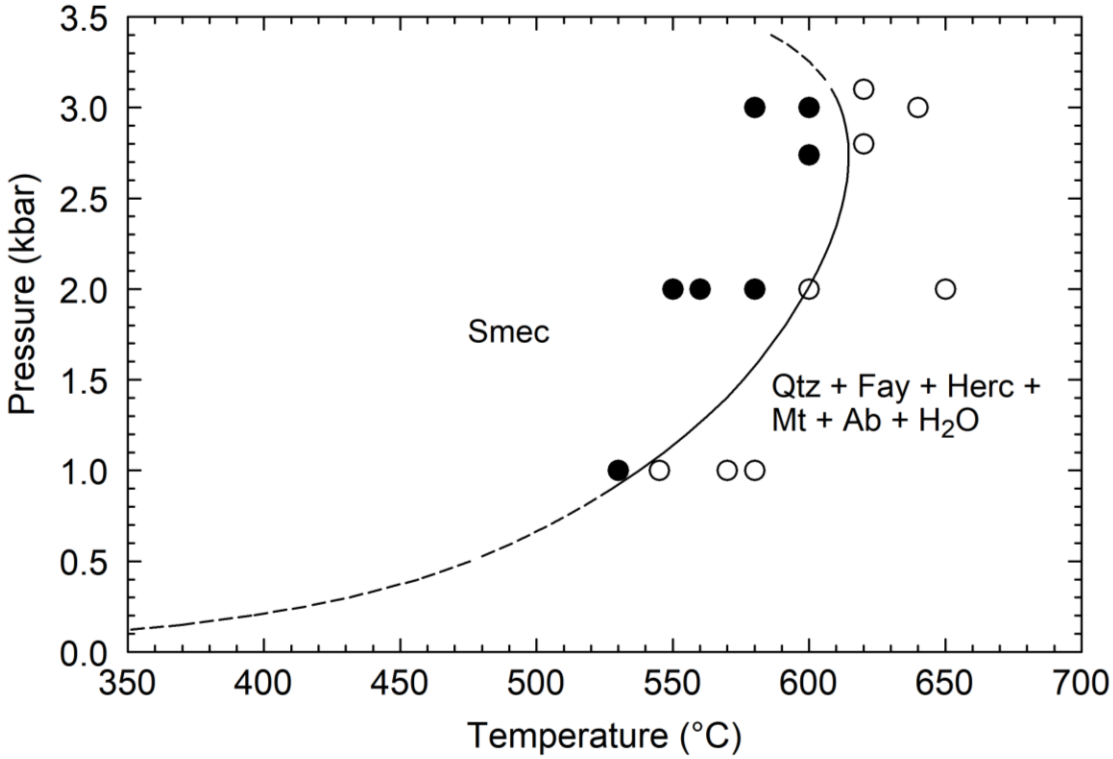
3.5
3.0
2.5
2.0
1.5
1.0
0.5
0.0
Pressure (kbar)
350
400
450
500
550
600
650
700
Temperature (°C)
Smec
Qtz + Fay + Herc +
Mt + Ab + H_2O

Figure 10

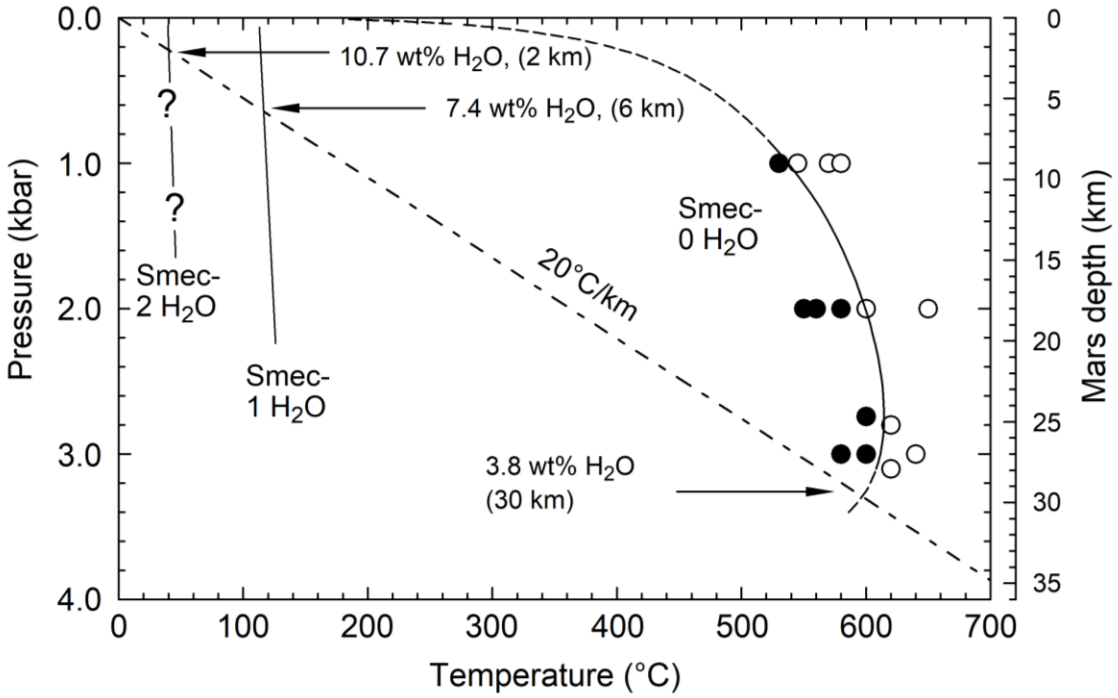
10.7 wt% H_2O, (2 km)
7.4 wt% H_2O, (6 km)
?
?
Smec-
2 H_2O
Smec-
1 H_2O
Smec-
0 H_2O
20°C/km
3.8 wt% H_2O
(30 km)
Pressure (kbar)
Mars depth (km)
Temperature (°C)
0.0
1.0
2.0
3.0
4.0
0
100
200
300
400
500
600
700
0
5
10
15
20
25
30
35

Figure 11

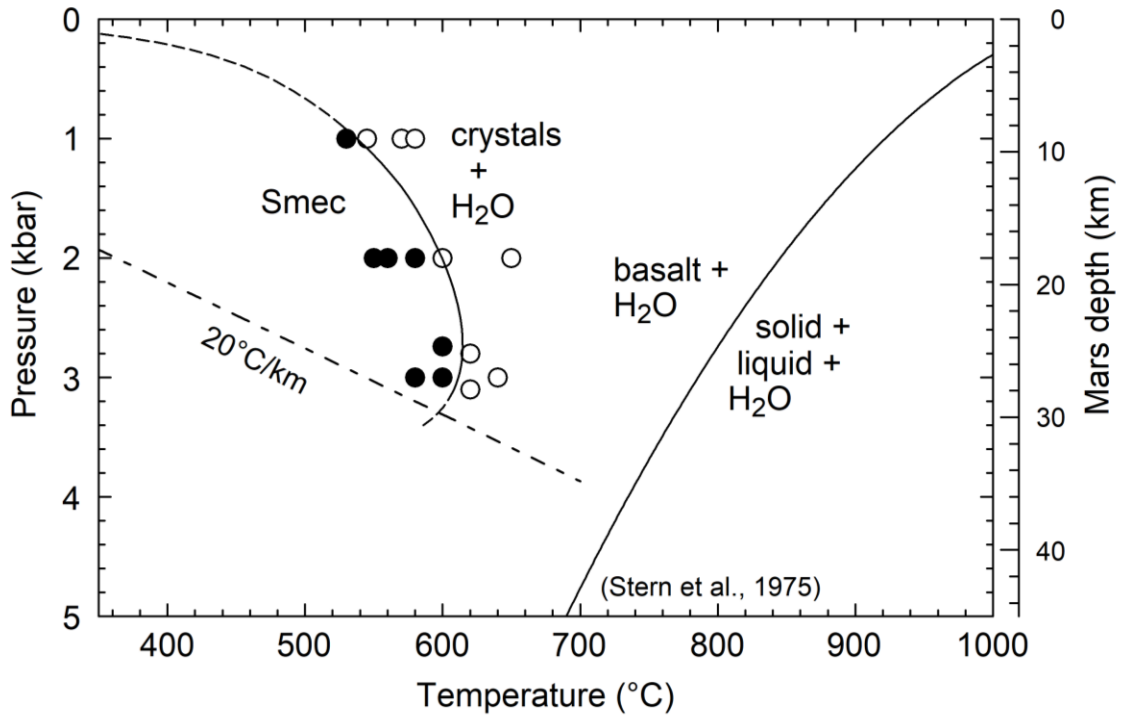
Pressure (kbar)
Mars depth (km)
Temperature (°C)
crystals
+
H_2O
Smec
basalt +
H_2O
solid +
liquid +
H_2O
20°C/km
(Stern et al., 1975)

\

Figure 12

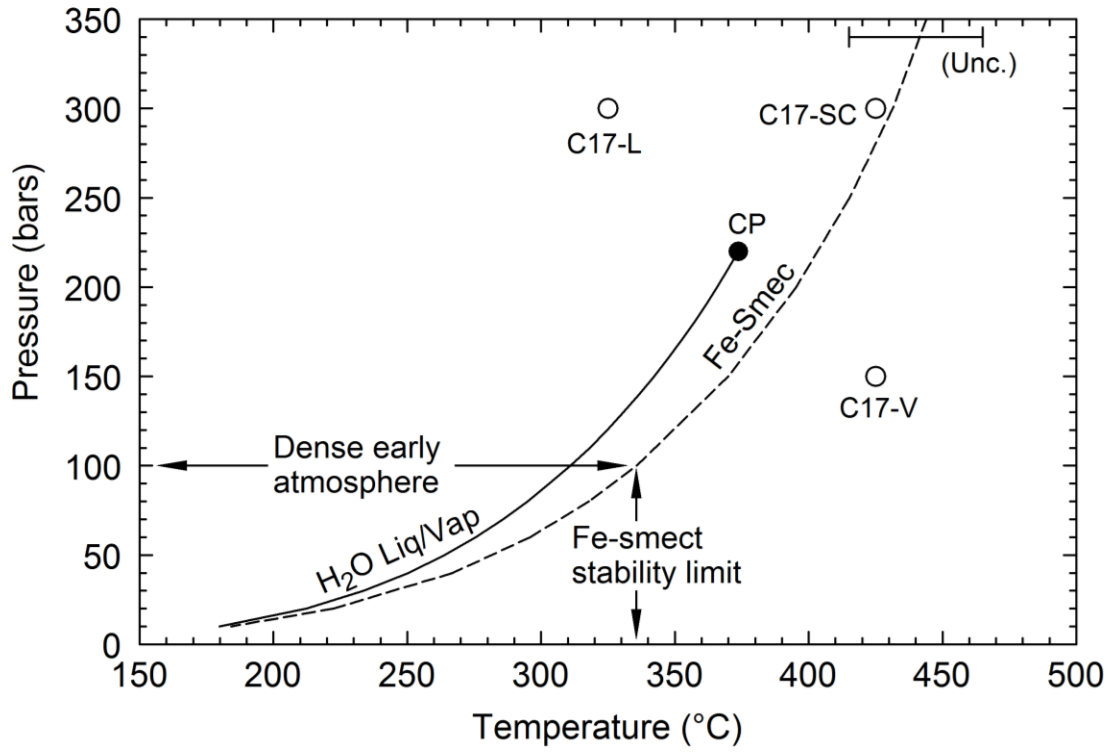
350
300
250
200
150
100
50
0
150
200
250
300
350
400
450
500
Pressure (bars)
Temperature (°C)
(Unc.)
C17-L
C17-SC
CP
Fe-Smec
C17-V
Dense early
atmosphere
H_2O Liq/Vap
Fe-smect
stability limit